Processes and flow over the Iceland-Faroe Ridge

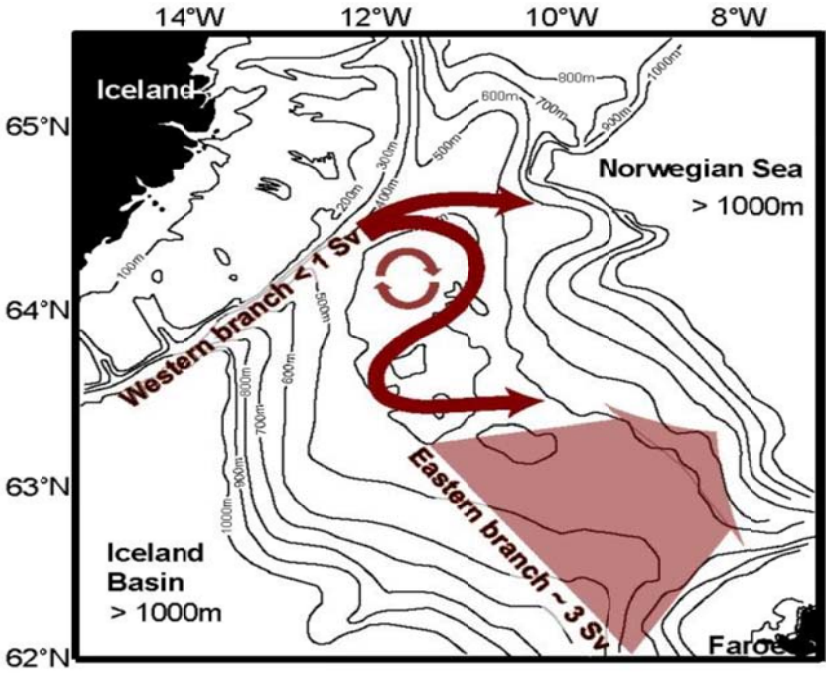

Pathways of Atlantic Water across the Iceland Faroe Ridge. Credits: Bogi Hansen (Havstovan)

Blue-Action: Arctic Impact on Weather and Climate is a Research and Innovation action (RIA) funded by the Horizon 2020 Work programme topics addressed: BG-10-2016 Impact of Arctic changes on the weather and climate of the Northern Hemisphere. Start date: 1 December 2016. End date: 28 February 2021.

The Blue-Action project has received funding from the European Union's Horizon 2020 Research and Innovation Programme under Grant Agreement No 727852.

About this document

Deliverable: D2.3 Processes and flow over the Iceland-Faroe Ridge
Work package in charge: WP2 Lower latitude drivers of Arctic change
Actual delivery date for this deliverable: 30 November 2019
Dissemination level: The general public (PU)

Lead authors
Danmarks Meteorologiske Institut (DMI): Steffen M. Olsen, Andrea Gierisch
Faroe Marine Research Institute (HAV): Karin M. H. Larsen, Bogi Hansen

Other contributing author(s)
National Oceanography Centre (NOC): Ben Moat

Reviewer
Danmarks Meteorologiske Institut (DMI): Chiara Bearzotti

We support Blue Growth!
Visit us on: www.blue-action.eu

Follow us on Twitter: @BG10Blueaction

Access our open access documents in Zenodo:
https://www.zenodo.org/communities/blue-actionh2020

Index

Summary for publication

Combining the results from the ester Valley Overflow field experiment with data from other in situ current measurements, from satellite tracked drifters, and from satellite altimetry, we find a consistent picture of the passage of Atlantic water across the Iceland-Faroe Ridge, which can be described in terms of two branches.

The Western branch passes through the Western Valley, where it is locked to the steep topography of the Icelandic slope, but part of it re-circulates back onto the ridge before entering the Norwegian Sea. It may have strong surface flow in a narrow current, but it is highly variable and its average volume transport is low. The Eastern branch passes the ridge as a broad flow with a core that shifts back and forth laterally (parallel to the ridge axis). In general, it exhibits weaker surface currents based on observations, but its volume transport is the dominant component and must be fairly stable to account for the stability of transport monitored at a section farther east.

The available data on Mean Dynamic Topography seem to reflect realistic large-scale circulation features, but to smear out the spatial structure of surface currents and transports. The Sea Level Anomaly data from satellite altimetry appear to be well related to surface currents in this region, at least on time scales from weeks to longer. When calibrated with the results from the WOW field experiment, they allow long-term monitoring of volume transport of the Western branch.

By applying a set of commentary modelling approaches, it is confirmed that the combined transport can be assessed and effectively monitored on a section north of the Faroes, disregarding that there is little model consensus on the strength of individual branches. Direct comparisons of model results and observations of the total transport show large discrepancies. Assessment of inherent model uncertainty for this and other inflow branches show that the Atlantic water flow across the Iceland-Faroe Ridge has a higher natural noise level and is less constrained by the applied forcing than could be expected. This new result puts emphasis on model ensemble approaches as the key to understand the climatic sensitivity of the system but also raises a concern about our capability to predict abrupt changes.

Results suggests that adequately tuned ocean models of eddy permitting resolution are sufficient for simulating the main characteristics of the Iceland-Faroe Ridge inflow including horizontal structure, individual characteristics of the two branches as well as seasonality of the net transport.

Work carried out

Work carried out relates to the tasks ***Task 2.1: Assessment of key lower latitude influences on the Arctic and their simulation*** in the Description of the Action.

Results from a nationally funded oceanographic field experiment, Western Valley Overflow (WOW) and other observations on the Iceland-Faroe Ridge (IFR) have been jointly analysed by partners HAV and DMI to develop a consistent observational based understanding of the flow across the Iceland-Faroe Ridge (IFR), its branches and strength. This includes integration also of earth observation assets like altimetry and mean dynamical topography.

Flow across the Iceland-Faroe Ridge has been shown to be strongly biased in global ocean and climate models in CMIP5/6 type configurations (partners DMI, HAV, NORCE, MRI). Assessments of additional ocean model simulations products have been conducted by partner DMI, HAV and NOC to further our

understanding of present model limitations (structural uncertainty or model inadequacy). We have targeted model resolution across the eddy permitting to eddy resolving domain as well as addressing the additional information derived from ensemble approaches (DMI and NOC).

Main results achieved

1. Introduction

The inflow of water from the Atlantic Ocean to the Nordic Seas occurs in three branches passing through the three main gaps between Greenland and Scotland, carrying warm and saline Atlantic water towards the Arctic and feeding the thermohaline processes generating the deep overflow waters (Østerhus et al., 2018). The strongest of these is the inflow between Iceland and the Faroes (IF-inflow, Figure 1.1a). The fate of this flow under a changing global climate is a question of huge societal importance, which can only be answered satisfactorily with climate models.

Before projections from a climate model can be relied upon, we need, however, to ensure that the model can reproduce essential features of reality and we have long been involved in comparing simulations from ocean components of such models with observations (Hansen 2015) that have been carried out on a section, the N-section, which crosses the Atlantic water flow where it has been focused into a fairly narrow boundary current, the Faroe Current (Figure 1.1b). So far, there has been little success in simulating the variations of this inflow branch, in contrast to the other two inflow branches.

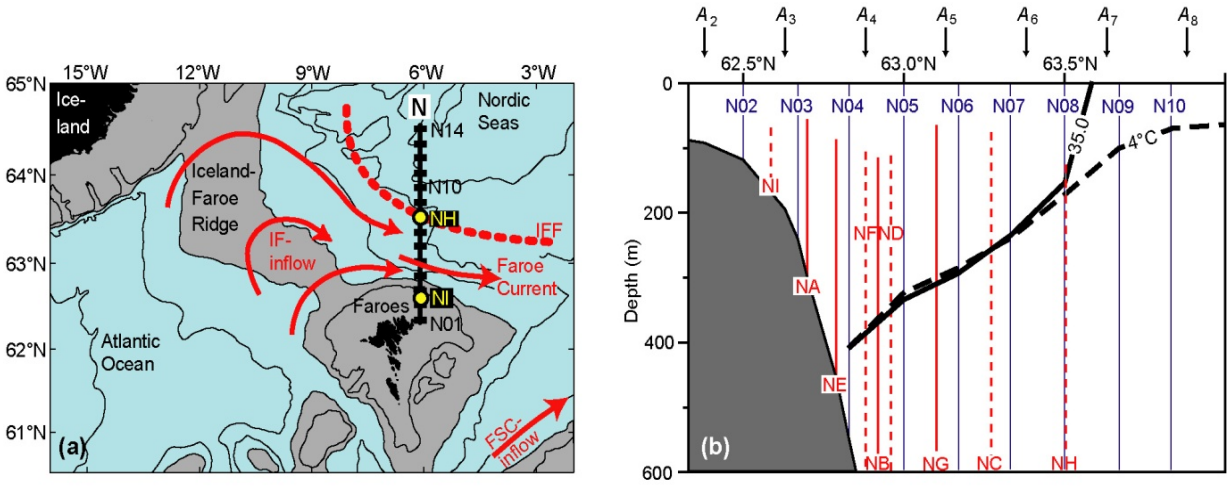

Figure 1.1. (a) The region between Iceland and the Scottish shelf with grey areas shallower than 500m. The two main Atlantic inflow branches are indicated by red arrows. The Iceland-Faroe inflow (IF-inflow) crosses the IFR, meets colder waters, termed Arctic water, in the Iceland-Faroe Front (IFF), and flows north of Faroes in the Faroe Current. The other main inflow branch (the FSC-inflow) is also shown. The black line extending northwards from the Faroe shelf is the N-section with CTD standard stations N01 to N14 indicated by black rectangles. Yellow circles indicate the innermost (NI) and the outermost (NH) ADCP mooring sites on the section. **(b)** The southernmost part of the N-section with bottom topography (grey). CTD standard stations are indicated by blue lines labelled N02 to N10. ADCP profiles are marked by red lines that indicate the typical range with continuous lines indicating the long-term sites. Altimetry grid points A_2 to A_8 are marked by black arrows and the thick black lines indicate the average depth of the 4 °C isotherm (dashed) and the 35.0 isohaline (continuous) on the section (from H2015).

Much of the inspiration for this task came from a study (Olsen et al. 2016), where Atlantic water volume transport of the Faroe Current, simulated by a low-resolution NEMO ocean model (ORCA 1 configuration resembling CMIP5 ocean modules), was compared with volume transport derived from the observations

(Hansen et al 2015). This intercomparison showed little similarity between simulated and observed volume transport. Instead, model simulations indicated that the water crossing the south-eastern part of the ridge was better correlated with the observations at the N-section. Observational results from the WOW field experiment gave new information, relevant to this question and it allow exploring this question further:

- Describe the Atlantic water inflow close to Iceland based on the observations from the WOW field experiment, satellite altimetry, and ocean- and climate-model configurations with enhanced resolution.
- Evaluate the coupling between the flow through the monitoring section and inflow branches across the Iceland-Faroe Ridge. Evaluate the representation of water mass transformation processes and quantify model uncertainty in heat transport towards the Arctic in relation to climate scenarios.

Here, we combine the current measurements on the IFR, acquired during the field phase of WOW, with other historic in situ current measurements, with data from satellite altimetry, and with data on satellite-tracked drifter buoys. This is done both to compare the different observational techniques and assess their accuracy and to describe the Atlantic water flow across the ridge. This observational description of the IFR is then combined with observational evidence from the N-section and compared with model simulations. In addition to the simulation reported in Olsen et al. 2016, we include additional model simulations and ocean analysis with better spatial resolution in the model-observation intercomparison.

2. Altimetry data

We use altimetry data both to complement in situ observations and to help interpret model results. Altimetry data were selected from the global gridded (0.25° × 0.25°) fields representing Mean Dynamic Topography (MDT) and daily averaged Sea Level Anomaly (SLA) available from Copernicus Marine Environment Monitoring Service (CMEMS) (http://marine.copernicus.eu). SLA values were selected for 8 grid points, which we label A_1 to A_8, along 6.125°W and 10 grid points, labelled S_1 to S_{10}, following the crest of the IFR (Figure 2.1). For each of these points, we have daily SLA values for 9292 days from 1 January 1993 to 10 June 2018, as well as (the constant) MDT values.

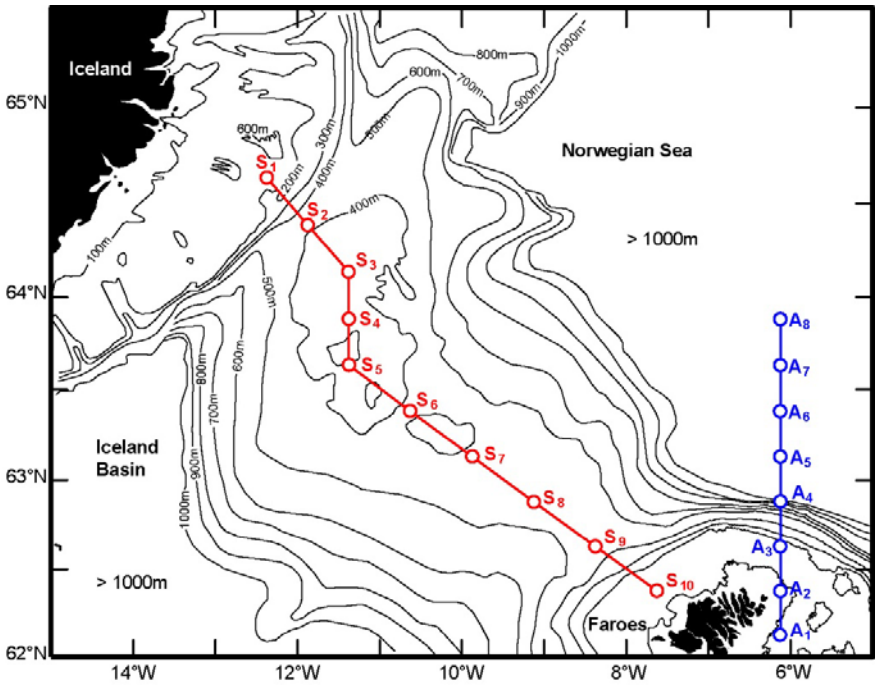

Figure 2.1 Altimetry grid points along two sections: 10 points following the crest of the IFR (red line and circles) and 8 points extending northwards from the Faroe shelf along 6.125°W, crossing the Faroe Current (blue line and circles).

The altimetry data on the N-section, A_1 to A_8, are discussed in Hansen et al. 2015. Here, we focus on the altimetry data over the crest of the IFR, S_1 to S_{10}, for which the details are listed in Table 2.1. Combining Mean Dynamic Topography (MDT) and average Sea Level Anomaly (SLA) in the grid points, we can calculate the differences in Sea Level Height (ΔSLH) according to these data sets (Table 2.1). If we assume geostrophic balance, the horizontally averaged surface velocity between two neighbouring grid points perpendicular to the connecting line may be determined as the ΔSLH-value multiplied by a factor $\alpha = g/(f \cdot L)$ where g is acceleration of gravity, f the Coriolis parameter, and L the distance between the two grid points. This estimate of the surface velocity is henceforth termed "altimetric velocity".

Multiplying the altimetric velocity by the distance between grid points, we get the volume transport in a unit vertical distance (1 m) of the water column. This parameter, which is a kind of transport density, is listed in Table 2.1 as HIV (Horizontally Integrated Velocity). The accumulated HIV over the whole ridge is seen to be $1.12 \cdot 10^4$ m^2 s^{-1}. If the flow was totally barotropic (not changing with depth) and bottom depth was constant, a depth of 340 m would give an average volume transport of 3.8 Sv, which is the average Atlantic water transport through the N-section (Hansen et al. 2015).

Table 2.1. Characteristics of the ten selected altimetry points for the period 1993.01.01-2017.12.31. Top three rows are at the points. Next nine rows are for intervals between neighbouring points. Average sea level height (Avg.SLH) is sum of MDT and average SLA-values. Direction is perpendicular to connecting line into the Norwegian Sea. α is the factor by which to multiply ΔSLH in order to get the altimetric velocity. HIV is Horizontally Integrated Velocity. Rows 11 and 12 show standard deviations of daily (Std.vel 1) and 31-day averaged (Std.vel 31) altimetric velocities. The bottom row shows correlation coefficients between neighbouring 31-day averaged altimetric velocities with statistical significance[1].

Point:	S_1	S_2	S_3	S_4	S_5	S_6	S_7	S_8	S_9	S_{10}
Latitude (°N):	64.625	64.375	64.125	63.875	63.625	63.375	63.125	62.875	62.625	62.375
Longitude (°W):	12.375	11.875	11.375	11.375	11.375	10.625	9.875	9.125	8.375	7.625
Avg.SLH (cm):	-33.5	-29.4	-25.4	-24.8	-25.6	-28.0	-26.0	-24.0	-20.6	-18.6
Distance (km):	36.8	36.9	27.9	27.9	46.6	46.9	47.1	47.4	47.7	
Direction (°):	49	49	90	90	37	36	36	36	36	
α (s^{-1}):	2.03	2.03	2.70	2.70	1.62	1.61	1.61	1.60	1.60	
ΔSLH (cm):	4.1	4.0	0.6	-0.9	-2.3	2.0	2.0	3.4	2.0	
Avg.vel (cm/s):	8.3	8.1	1.7	-2.3	-3.8	3.2	3.1	5.5	3.2	
HIV(m^2 /s):	3060	2998	476	-643	-1767	1484	1480	2586	1526	
Accum. HIV(m^2 /s):	3060	6058	6534	5891	4123	5607	7087	9673	11199	
Std.vel 1 (cm/s):	5.3	3.8	5.0	4.3	5.0	5.3	5.2	5.1	4.6	
Std.vel 31 (cm/s):	1.7	1.2	1.3	0.9	2.1	2.1	2.2	2.1	1.8	
Corr. Coeff. :	0.40***	0.10	0.62***	0.12	0.06	-0.05	-0.32***	0.05		

The general features of the circulation in the region indicated by the MDT are shown in Figure 2.2 with inflow (to the Norwegian Sea) in both ends of the ridge and a partial re-circulation just north of mid-ridge.

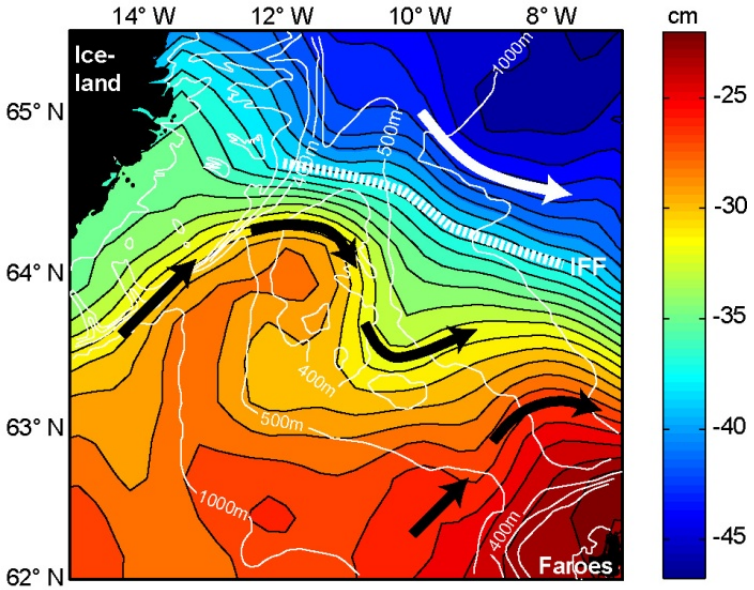

Figure 2.2. The Mean Dynamic Topography (background colours) above the IFR according to altimetry data from Copernicus Marine Environment Monitoring Service (CMEMS). Isobaths are shown by thin white lines for every 100 m down to 500 m and for 1000 m depth. Black arrows indicate the two main Atlantic inflow regions over the IFR. The white arrow indicates the surface circulation of the Norwegian Sea. The thick hatched white line indicates the Iceland-Faroe Front (IFF).

[1] Here and elsewhere statistical significance is indicated by asterisks: "*" indicates $p<0.05$, "**" indicates $p<0.01$, "***" indicates $p<0.001$. Significance levels are corrected for serial correlation according to Pyper and Peterman (1998).

3. ADCP measurements on the IFR
3.1 ADCP deployments

At four different sites on the IFR, Acoustic Doppler Current Profilers (ADCPs) have been deployed in trawl-protected bottom-mounted frames over extended periods. The four deployments are labelled A, B, C, and W and details of the deployments are listed in Table 3.1. For daily averaged ADCP velocities, the data quality is normally 100% from the deepest bin (bin 1) up to a bin (the Top bin) listed in Table 3.1, which is often deeper than the highest bin recorded by the ADCP (the Last bin).

Table 3.1. Characteristics of the four ADCP deployments on the IFR. Last bin indicates the shallowest level in the data set. Top refers to the shallowest level with 100 % good daily averaged ADCP data.

ADCP site:	A	B	C	W
Latitude (°N):	62.635	62.861	62.763	64.445
Longitude (°W):	8.453	8.589	9.712	12.063
Bottom depth (m):	498	495	497	402
Depl. Start:	2004.09.07	2003.07.05	2004.07.04	2016.08.15
Depl. End:	2005.05.23	2004.06.10	2005.05.23	2017.05.19
Duration (days):	259	342	324	278
Last bin:	44	44	43	30
Top bin:	44	43	42	26
Top depth (m):	50	55	69	135
Top speed (cm/s):	7.8	9.8	7.3	22.1
Top direct. (°):	88	38	94	73

To allow calculation of volume transport, the velocity profile has to be extended all the way to the surface. This is normally done in two steps, first from the Top bin to the Last bin, then from the Last bin to the surface. For the first step, we need to extrapolate those records for which some bins between the Top bin and the Last bin were error flagged. The method for doing that is based on the fact that neighbouring bins in these cases generally are highly correlated as exemplified in Table 3.2. Zero-offset regression factors are first determined from the good data and then used to extrapolate for the error-flagged data (see Table 2 in Hansen et al., 2003 for more details). The second step involves extrapolating from the Last bin up to the surface. Here, we approximate and simply extend the velocity at the Last bin up to the surface unchanged.

Table 3.2. Correlation coefficients and regression (zero-offset) factors between neighbouring bins for ADCP deployment W.

		Eastward velocity		Northward velocity	
Bins	Days	Corr.	Factor	Corr.	Factor
26-27	277	0.993***	1.024	0.986***	1.033
27-28	269	0.987***	1.011	0.986***	1.027
28-29	256	0.983***	1.034	0.974***	1.058
29-30	240	0.980***	1.024	0.962***	1.045

3.2 Combining ADCP data and altimetry

The average surface velocities for the four ADCP deployments are illustrated by the blue arrows in Figure 3.1, which also shows the average altimetric velocities (Table 2.1) between the nine pairs of neighbouring grid points (red arrows). The two sets of arrows have the same general directions, but not magnitudes. Even if we assume the MDT (and hence geoid) to be accurately determined, a quantitative match between the two sets was not to be expected, however, since the ADCPs measure velocity at one geographical point, whereas the altimetric velocity is horizontally averaged over the interval between the two altimetry grid points.

If, instead of averages, we consider variations in surface velocity, the uncertainty associated with the MDT is removed, but the difference between the point measurement of the ADCP and the horizontal average derived from altimetry remains. Also, the ADCPs do not profile all the way to the surface. We would therefore not expect a perfect relationship, even if data quality was perfect.

Nevertheless, we do find statistically significant correlation coefficients, especially for sites B and W (Table 3.3) when the velocity of the uppermost (Top) bin with high quality is correlated with ΔSLH variations represented by SLA values.

Table 3.3. Correlation coefficients between weekly averaged ADCP velocity at the top bin and ΔSLH between neighbouring altimetry points.

Altimetry interval:	S_1-S_2	S_2-S_3	S_3-S_4	S_4-S_5	S_5-S_6	S_6-S_7	S_7-S_8	S_8-S_9	S_9-S_{10}
ADCP A tow. 36°:	n.s.	n.s.	n.s.	n.s.	n.s.	n.s.	-0.49**	n.s.	0.45*
ADCP B tow. 36°:	n.s.	n.s.	n.s.	n.s.	n.s.	n.s.	n.s.	0.64***	n.s.
ADCP C tow. 36°:	n.s.	n.s.	n.s.	n.s.	n.s.	n.s.	0.44*	n.s.	n.s.
ADCP W tow. 49°:	0.89***	n.s.	-0.69***	-0.51**	n.s.	n.s.	n.s.	n.s.	n.s.

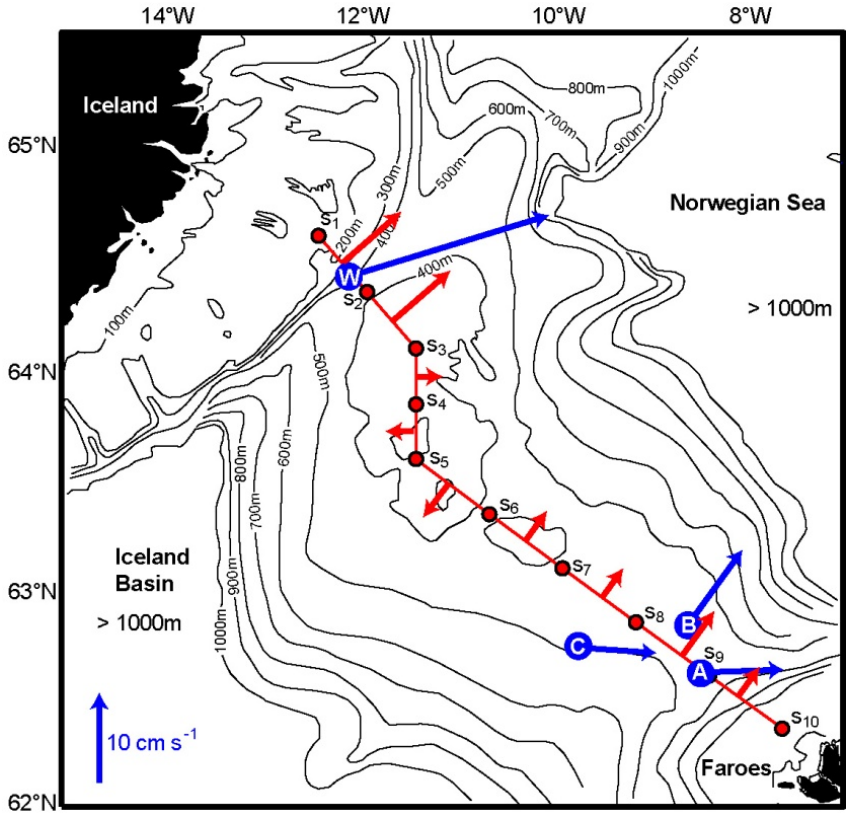

Figure 3.1. Positions of the four ADCP deployments are shown by blue circles. Blue arrows indicate average velocity for the top bin with 100% good daily averaged velocity data. Red arrows indicate average altimetric velocity (based on MDT+SLA). The velocity scale is in the lower left corner.

Taking into account the above-mentioned differences between ADCP velocities and altimetric velocities, the high positive correlation for deployment W and altimetry interval S_1-S_2 in Table 3.3 is noteworthy. The high correlation is maintained when we use the ADCP velocity extended all the way to the surface (Table 3.4), but the regression factor, α_v, was found to be 7.5 s^{-1}, which is more than three times higher than expected from geostrophy (2.03 s^{-1}, Table 2.1).

Table 3.4. Correlation and regression coefficients between ΔSLH and two parameters derived from ADCP measurements at sites B and W. Surface velocity (v) is component towards the direction specified (Dir.). VIV (q) is defined as the vertical integral of velocity towards the direction specified (Dir.) from the surface down to the level where it first becomes zero. Regression coefficients are defined as: $v(t)=\alpha_v \cdot \Delta SLH(t)+\beta_v$ and $q(t)=\alpha_q \cdot \Delta SLH(t)+\beta_q$.

				Surface velocity versus ΔSLH			VIV versus ΔSLH		
ADCP	Dir.	Altim. interv.	Weeks	Corr.	α_v s^{-1}	β_v cm s^{-1}	Corr.	α_q m s^{-1}	β_q m^2 s^{-1}
B	36°	S_8-S_9	48	0.60***	1.9±0.8	7.1±2.2	0.67***	723±243	38.7±7.1
W	49°	S_1-S_2	39	0.87***	7.5±1.4	12.1±3.4	0.88***	2045±381	36.8±9.1
W	49°	S_1-S_3	39	0.80***	5.9±1.5	8.6±4.8	0.83***	1646±374	26.8±12.0

The altimetry is related to the surface velocity horizontally averaged between the two altimetry points. The high correlation therefore implies that the surface velocity at site W must be approximately proportional to the horizontally averaged velocity. The high value for the regression coefficient, α_v, then implies that the proportionality factor is much higher than one, which again implies that the core of the current must be considerably narrower than the altimetry interval.

We therefore conclude that most of the flow between altimetry points S_1 and S_2 is confined to a narrow current with a core close to site W, which does not move appreciably along the altimetry section presumably due to the steep topography of the Icelandic slope on the northeastern flank of the current. To give the measured regression coefficient, α_v, the "equivalent width" of this current (Figure 3.2) has to be less than one third of the distance between S_1 and S_2, i.e. ≈ 10 km (36.8 · 2.03/7.5 km).

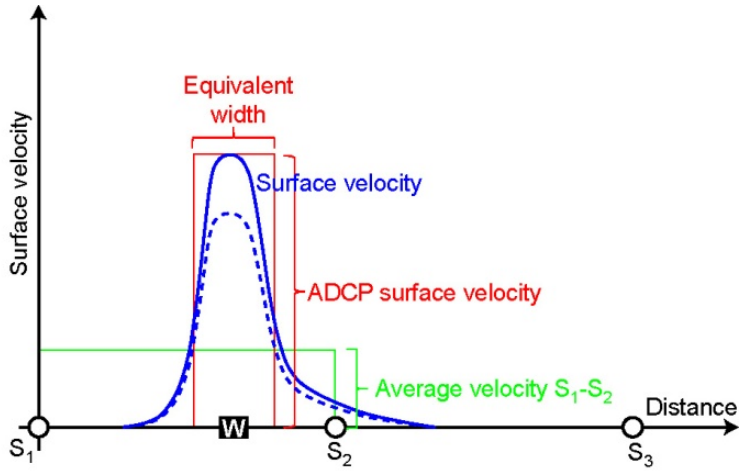

Figure 3.2. Schematic drawing illustrating the definition of equivalent width for a narrow current that does not move laterally. The continuous blue curve illustrates the lateral (along altimetry section) variation of the surface current on a specific day. The green rectangle illustrates the horizontally averaged velocity for altimetry interval S_1-S_2 on the same day. The equivalent width based on this interval is defined such that the red and the green rectangles have the same area. The dashed blue curve shows velocity on another day illustrating that the current varies in strength, but does not move laterally.

If this interpretation is correct, we may estimate the average surface velocity component perpendicular to the altimetry section between S_1 and S_2 by multiplying the ADCP surface component by the ratio between current width and interval length (10/36.8). This would give an average velocity around 5.5 cm s^{-1}, which is considerably less than the 8.3 cm s^{-1} indicated by the MDT (Table 2.1). As will be argued in Sect. 3.4, the small-scale variations of the MDT are, however, questionable.

According to Table 3.3 the correlation coefficient between ADCP top velocity at site W and ΔSLH for interval S_2 - S_3 is not significant (R = 0.14 for weekly averages). Nevertheless, the southeastern flank of

this current probably extends into the interval between S_2 and S_3. This is indicated both by the significant correlation between the altimetric velocities in these two intervals (last row in Table 2.1) and by the high correlation in the last row of Table 3.4. If we use this interval, S_1-S_3, and the values in the last row of Table 3.4, the equivalent width becomes 13 km instead of 10 km. Since S_1-S_2, is better correlated with the ADCP velocity at site W than S_1-S_3, we will in the following use 10 km for the width.

3.3 Volume transport

When we know the width of the current associated with the ADCP at site W then an approximate value for the volume transport of Atlantic water across the ridge in this area – i.e. between altimetry points S_1 and S_2 - may be calculated by multiplying the vertically integrated velocity from the extended ADCP data by this width. With only velocity data and no information on the temperature or salinity profiles, it is not obvious, how to determine the depth interval, over which to integrate the velocity (towards 49°) profile, but we will focus on the "Vertically Integrated Velocity (*VIV*)", defined as:

$$VIV(t) = \int_0^{D_0(t)} U(z,t)dz \qquad (3.1)$$

where *U(z,t)* is the velocity component perpendicular to the altimetry section over the site at depth *z* and time *t* and $D_0(t)$ is the depth, at which *U(z,t)* first becomes zero. Multiplying this parameter for site W by a width of 10 km, we get the red curve in Figure 3.3a. A second alternative, shown by the blue curve, is to integrate over almost the full water column (from surface down to the centre depth of bin 1). A third alternative - integrating all positive velocities - would be almost identical to the red curve (not shown).

Since the blue curve presumably includes some overflow water going the opposite way, we will use the red curve, which indicates that the average volume transport of Atlantic water between S_1 and S_2 is highly variable. For short periods, this flow seems to exceed 3 Sv, which is almost equal to the average Atlantic water transport through the N-section, but most of the time, the flow is much weaker and the average is only around 0.6 Sv.

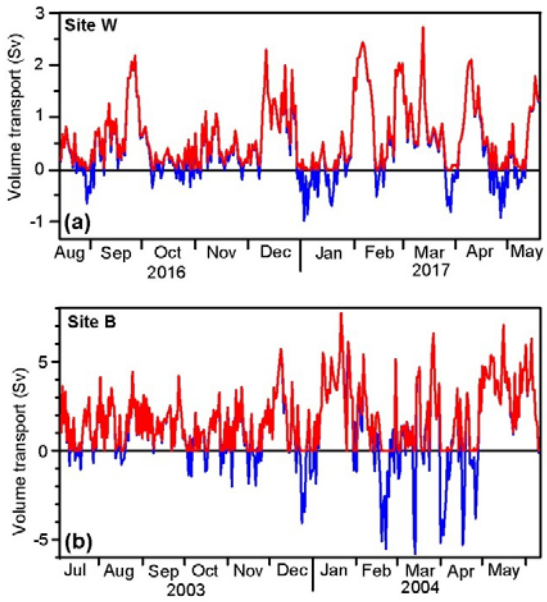

Figure 3.3. Volume transport of the Atlantic inflow current over ADCP site W (towards 49°) **(a)** and over site B (towards 36°) **(b)** during the deployment periods assuming that the widths of the currents are 10 km and 40 km, respectively. Blue curves show transport from the surface down to the deepest ADCP bin. Red curves show transport from the surface down to the level where the velocity first becomes zero. If the surface velocity is negative, the red curves are zero.

A similar argument may be used for the ADCP velocities from site B. There the regression factor (1.9 s^{-1} from Table 5) is much closer to the theoretical value (1.6 s^{-1} in Table 3) and the width is found to be around 40 km (no steep topography). Using this value, the volume transport between points S_8 and S_9 may be calculated from the ADCP data for the deployment period (Figure 3.3b).

Since the velocity variations demonstrate a highly barotropic character (Table 3.2), it seems likely that not only surface velocity, but also the whole velocity profile, and hence also the integral *VIV(t)*, might be well correlated with the local along-section ΔSLH as derived from altimetry. As demonstrated in Table 3.4, that is indeed the case for deployment W and to some extent also deployment B. The regression coefficients in Table 3.4 may therefore be used to reproduce the temporal variation of *VIV(t)* for the whole altimetry period. Time series of volume transport may then be derived by multiplying *VIV(t)* by the respective widths and lowpassed values are shown by the blue and the green curves in Figure 3.4. The red curve in Figure 3.4 is the lowpassed volume transport of Atlantic water through the N-Section (Hansen et al. 2015).

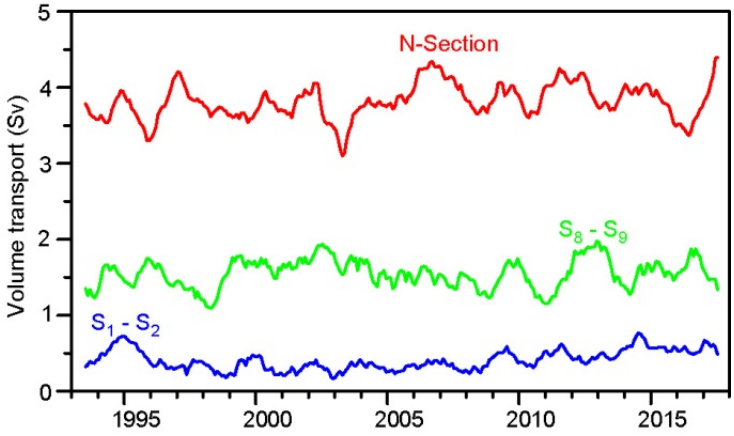

Figure 3.4. Lowpassed (12 month running mean) volume transport of the Atlantic inflow current between altimetry points S_1 and S_2 (over ADCP site W, blue), the volume transport of the Atlantic inflow current between S_8 and S_9 (over ADCP site B, green), and the Atlantic water flow through the N-Section (red).

3.4 Where does the Atlantic water cross the ridge?

A priori, the most comprehensive data set for determining the average surface flow field should be the gridded Mean Dynamic Topography (MDT), illustrated in Figure 2.2, and the geostrophic velocities derived from it, illustrated by the red arrows in Figure 3.1. From Table 2.1, the accumulated horizontally integrated velocity (HIV), based on this, is $1.12 \cdot 10^4$ m^2 s^{-1}, which as previously mentioned implies that an average depth of 340 m would give a transport of 3.8 Sv equal to what has been measured through the N-section.

According to Table 2.1, more than half of the accumulated HIV occurs between altimetry points S_1 and S_3 although part of it recirculates farther south on the ridge (Figure 2.2). Since the northern half of the ridge is shallower than the southern half, this cannot be directly converted to volume transport, but still argues that a substantial fraction should cross the ridge between S_1 and S_3.

This conclusion, based on the MDT, is not consistent with the ADCP measurements at site W and their link to the SLA variations. From them, we concluded that the average Atlantic water transport between S_1 and S_2 was only 0.6 Sv during the ADCP measurements (Figure 3.3a) and only 0.4 Sv over the whole altimetry period (Figure 3.4). The high correlation between the ADCP velocity and ΔSLH across the interval $S_1 - S_3$ (last row in Table 3.4), together with the increase in current width calculated from this (from 10 km to 13 km), furthermore argues that the only Atlantic water flow between points S_2 and S_3 is from the southeastern flank of the current through the Western Valley, perhaps increasing the total long-term average transport between S_1 and S_3 to approximately 0.5 Sv.

This discrepancy between the MDT and ADCP measurements is consistent with the results for the N-section, where it was found (Hansen et al. 2015) that the change in sea level across the whole width of the Faroe Current (point A_2 to point A_8 in Figure 2.1) determined from the MDT was fairly close to (within 20%) the value derived from ADCP measurements. On smaller spatial scales, on the other hand, the MDT appeared to be too smooth. Thus, the difference in MDT between points A_3 and A_5, where most of the transport is focused, was less than two thirds of the difference based on ADCP measurements (Hansen et al. 2015).

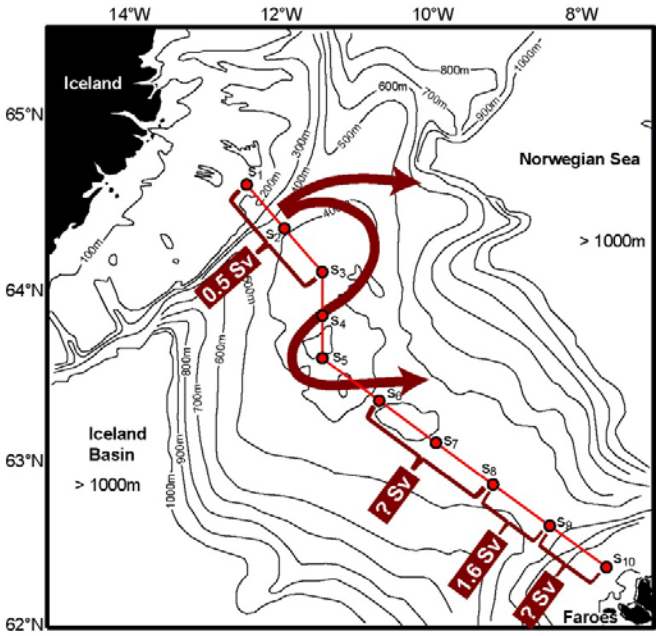

Figure 3.5. Sketch illustrating the regions where Atlantic water is likely to cross the IFR based on ADCP observations and sea level anomaly (SLA) data from satellite altimetry.

We therefore do not rely on the small-scale variations in the MDT, which is reflected in the sketch in Figure 3.5 where we have attempted to synthesize the information from the ADCP and altimetry measurements into a coherent picture. In this sketch, we have only 0.5 Sv passing through the Western Valley on average, as argued above, although the relative uncertainty of this value is probably high.

As indicated by the thick curved brown arrows on Figure 3.5, a substantial part of the flow through the Western Valley seems to recirculate back towards the Iceland Basin before once again turning eastwards. Partly, this is based on the structure of the MDT as shown in Figure 2.2, but it is also supported by the highly significant negative correlations between the ADCP velocity at site W and ΔSLH across the intervals $S_3 – S_4$ and $S_4 – S_5$ (Table 3.3)

In this framework, only a small fraction of the Atlantic water crosses the northern half of the ridge on average. If we assume no major change in Atlantic water transport between the ridge and the N-Section, more than 3 Sv must then cross the southeastern half of the ridge. Apparently, half of that (1.6 Sv) crosses between S_8 and S_9. The remainder must on average cross between S_6 and S_8 and/or between S_9 and S_{10}, as indicated by the question marks in Figure 3.5. From the correlations between altimetry and ADCP A in Table 3.3, it seems that these two contributions may be anticorrelated.

We furthermore find that the top bin velocity of the ADCP at site B is also anticorrelated with ΔSLH across the interval $S_6 – S_8$ (R = -0.51** for weekly averages). Most likely, there is a flow across the south-eastern half of the ridge with a fairly steady volume transport around 3 Sv, which meanders laterally in the interval between altimetry points S_6 and S_{10}, but not as initially hypothesized a strong compensation between eastern and western inflow branches (Olsen et al. 2016).

4. Satellite-tracked drifter data

Quality controlled data, interpolated to 6-hour intervals, from satellite-tracked drifter buoys in the area (0°-30°W, 50°N-65°N) were downloaded from NOAA's Atlantic Oceanographic and Meteorological Laboratory (AOML) (http://www.aoml.noaa.gov/envids/gld/dirkrig/parttrk_spatial_temporal.php). The drifters are drogued at 15 m depth and only data with the drogue attached are used here. A total of 854 drifters were deployed in or entered the area and less than one tenth of these passed into the Norwegian Sea through the gap between Iceland and Scotland, 47 over the IFR, and 34 south of the Faroes (Figure 4.1).

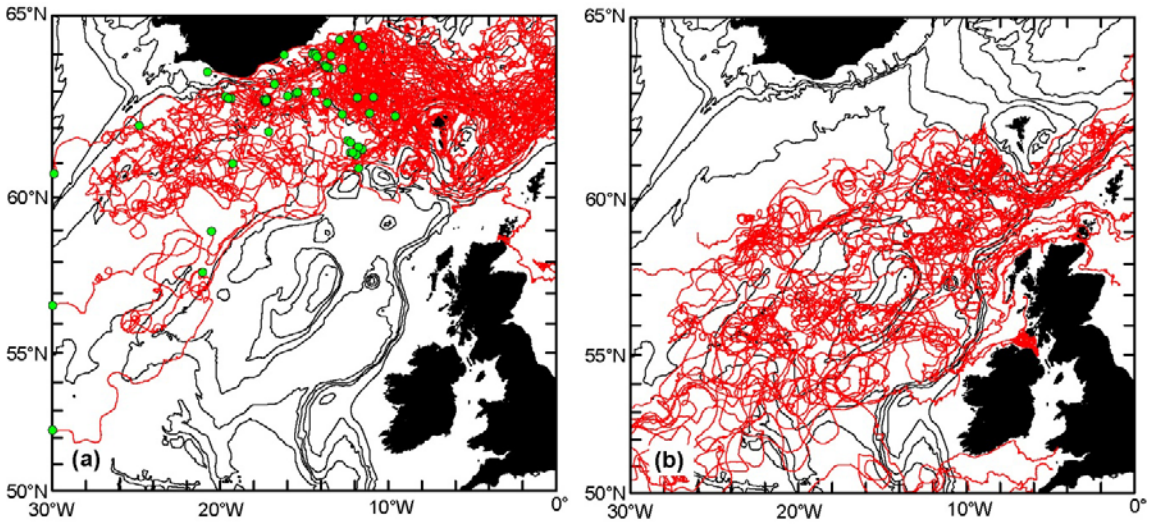

Figure 4.1. Tracks (red curves) of drifters passing into the Norwegian Sea between Iceland and Scotland. **(a)** Drifters crossing the IFR, green circles indicate position of deployment or where on the boundary the drifter entered the area. **(b)** Drifters entering the Norwegian Sea south of the Faroes.

The drifters passing south of the Faroes (Figure 4.1b) came from areas in the Rockall Trough, over the Rockall-Hatton Plateau, and from the south-eastern part of the Iceland Basin, but all the drifters crossing the IFR (Figure 4.1a) came from the Iceland Basin or the north-western slope of the Rockall-Hatton Plateau.

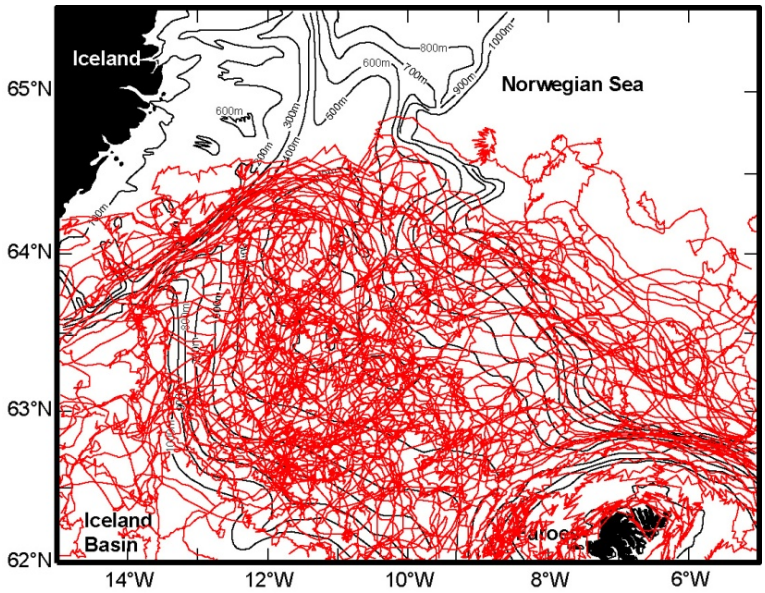

Figure 4.2. Drifter tracks across the IFR.

If we look closer at the drifter paths across the IFR (Figure 4.2), it appears as if drifters have covered almost every area above the ridge. To look for regularities, the drifter tracks were first averaged to daily positions to reduce the scatter and then grouped according to the location where they first crossed the altimetry line (Figure 4.3).

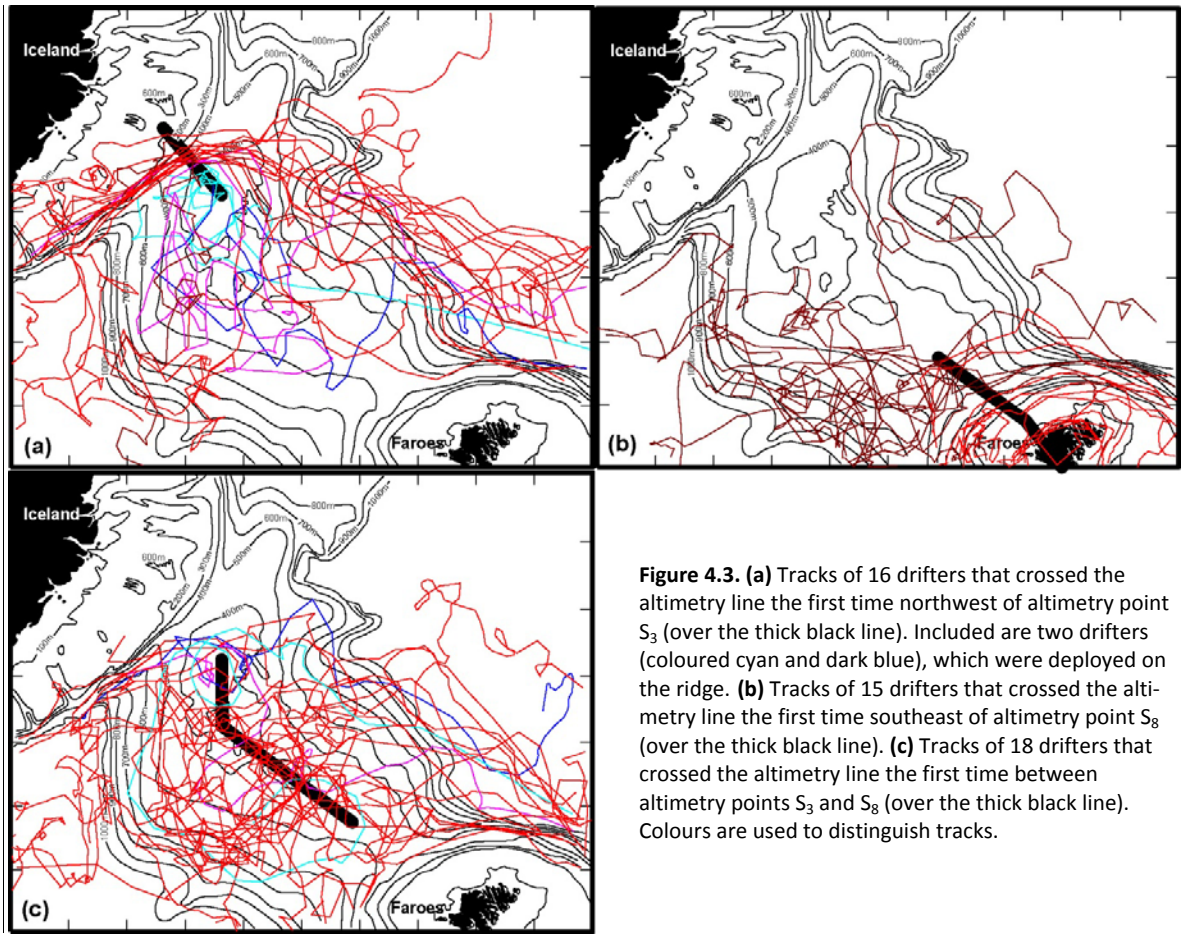

Figure 4.3. (a) Tracks of 16 drifters that crossed the altimetry line the first time northwest of altimetry point S_3 (over the thick black line). Included are two drifters (coloured cyan and dark blue), which were deployed on the ridge. **(b)** Tracks of 15 drifters that crossed the altimetry line the first time southeast of altimetry point S_8 (over the thick black line). **(c)** Tracks of 18 drifters that crossed the altimetry line the first time between altimetry points S_3 and S_8 (over the thick black line). Colours are used to distinguish tracks.

From Figure 4.3 it appears that drifters passing close to or over the Icelandic or Faroese slopes travelled along fairly straight paths, whereas the drifters that crossed the ridge closer to the middle were more affected by eddying motion. This is especially noteworthy over the Western Valley, which is bounded by the Icelandic slope on its north-western side. There, Figure 4.3a indicates a "highway" for drifters where they flow along almost straight lines parallel to the topography.

This behaviour is consistent with the high near-surface velocity indicated by the ADCP at site W (longest blue arrow in Figure 3.1) and Figure 4.3a indicates that many drifters have followed this path. This is confirmed in Figure 4.4a, which shows that 20 drifters, i.e. 43% of the total 47, crossed the altimetry line northwest of point S_4.

A priori, this might seem to contradict Figure 3.5, which had only 0.5 Sv of Atlantic water through this gap, but this is not necessarily a contradiction. Firstly, there is no guarantee that the deployment positions of the drifters have a representative distribution within the source waters for the IF-inflow. From the green circles in Figure 4.1a, it appears that relatively many drifters have been deployed into the boundary flow south of Iceland that feeds the inflow through the Western Valley.

Secondly, a high number of drifters passing through a gap in the surface does not necessarily imply a high volume transport through that gap. That will depend on the bottom depth and the region around the Western Valley is considerably shallower than the southeastern part of the ridge. The vertical variation of the velocity also plays a role. For an ADCP record, we may define an "equivalent depth" as the ratio between the average value for *VIV(t)*, as defined by Eq. (3.1), and the average surface velocity. For the deployment at site W, this parameter was 288 m, whereas it was 510 m for the deployment at

site B. Thus, a given surface velocity at site B can be expected to imply almost twice as much volume transport as the same velocity at site W.

Thus, the large number of drifters through the Western Valley do not necessarily imply that the small volume transport for that region in Figure 3.5 is much too low, although it might argue for a limited increase. There are also several drifters in Figure 4.3a that show a path consistent with the partial re-circulation in Figure 2.2 and Figure 3.5 and we note that some of them (dark blue and cyan tracks in Figure 4.3a,c) make complete circles in a location close to altimetry point S_3, indicating the existence of a quasi-permanent eddy in this area.

The drifter data allow us to estimate the time that near-surface Atlantic water requires to cross the IFR. For that purpose, the thick green lines in Figure 4.4a were used to define the boundary of the IFR. On average, the duration of a drifter within this boundary was 64 days, but more than 40% of the drifters crossed this area within less than 30 days (Figure 4.4b).

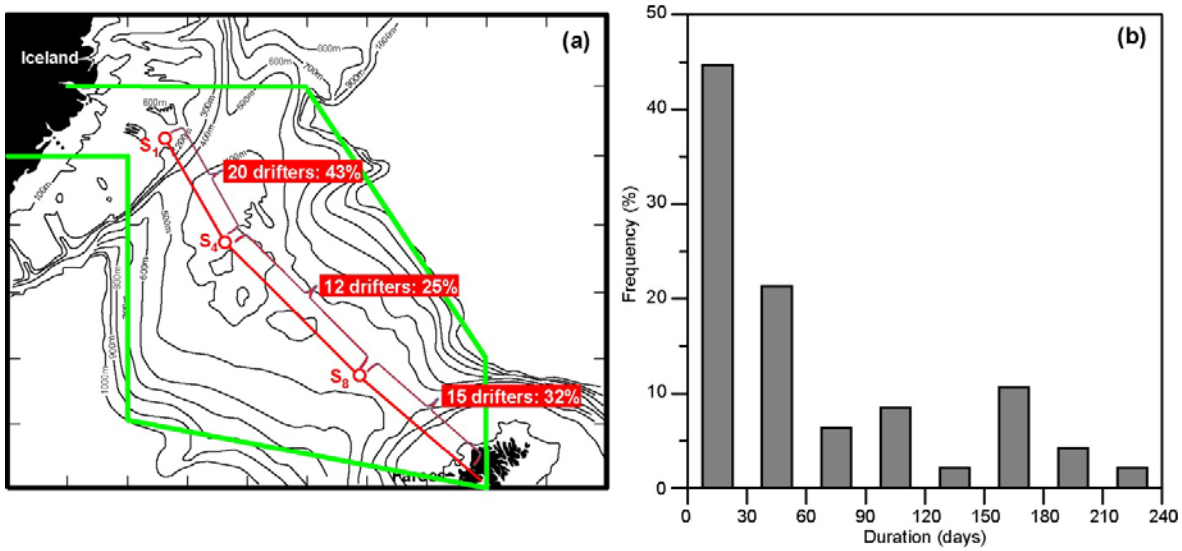

Figure 4.4. (a) Thick green lines bound the region defined as the ridge. Red lines show three gaps between altimetry points and indicate how many drifters passed through each gap. **(b)** Frequency distribution of the duration that drifters spent over the ridge (within the thick green lines on **(a)**).

5. Model - observation intercomparison

As indicated in the introduction, much of the motivation for this study came from simulations with a low-resolution NEMO ocean model (Olsen et al. 2016) representative from CMIP5 ocean configurations. Here, we will look in more detail at these simulations, as well as results from other models with higher resolutions and ocean analysis products. We will focus on the intercomparison between the model simulations and observations without going into the modelling details.

5.1 Intercomparison criteria

The basic question motivating the intercomparisons is to what extent the model simulations reflect realistic features of the warm and saline Atlantic water passing between Iceland and Faroes. To that aim, we compare the model simulations with values independently derived from observations. The derivation of the observational results does, however, involve both assumptions and approximations (Hansen et al. 2015). A priori, lack of similarity between model and observations may therefore derive from observational uncertainty as well as from ocean modelling uncertainty, the latter including structural limitations in model configuration in part connected to resolution, but also uncertainties in the model input and forcing data. The latter can to some extend be addressed by using ensemble results from ocean analysis.

To account for this, we use three different criteria for the comparison. The first of these is the volume transport of Atlantic water through the N-section. The second is the pathway of Atlantic water across the IFR – how much crosses the ridge over the northern/southern part. The third criterion is the sea level tilt across the Faroe Current as it passes through the N-section.

For the first criterion, simulated volume transport is compared with observed transport, calculated as described in Hansen et al. 2015. For the other two criteria, model simulations are compared with altimetry data. In Sect. 3, we have argued that the Mean Dynamic Topography data in this region do not have the necessary spatial resolution, but that the sea level anomalies (SLA-values) over the IFR are consistent with the (arguably few) ADCP measurements.

For the N-section, the quality of the altimetry SLA-data has been assessed by Hansen and Larsen (2019), by comparison with ADCP measurements at four long-term deployment sites (NA, NE, NB, and NG in Figure 1.1) located between altimetry points A_3 and A_5. For 94 monthly (28-day) averages, the correlation coefficient between the ΔSLH difference across this interval and a linear combination of surface velocities from these four ADCP sites was 0.86***. This interval is where most of the Atlantic water transport through the section is focused and ΔSLH differences largest. Over the rest of the N-section, the ADCP measurements are not sufficiently comprehensive for a similar check, but there should be no reason for a much worse fit.

Since SLA-data from altimetry enter into the derivation of observational estimates of volume transport (Hansen et al. 2015), these three criteria are not completely independent, but the surface velocities derived from ADCP measurements are completely independent of the altimetry data. The good fit between these two data sets is therefore a strong indicator that both of them reflect reality to a high degree. Since the ΔSLH difference between two altimetry points represents the horizontally averaged surface velocity between these points, we therefore consider the third criterion – sea level tilt across the Faroe Current – as the most decisive criterion for evaluating how well a simulation reflects the variations of this current.

5.2 Intercomparison for the low-resolution NEMO model

As detailed in Olsen et al. 2016, this ocean configuration of NEMO (Nucleus for European Modelling of the Ocean) has a resolution of 1°×1° with a meridional refinement to 1/3° at the equator, referred to as the ORCA1 grid. The uncoupled simulation for the period 1948-2011 was forced by 6-hourly atmospheric NCEP reanalysis data (Kalnay et al., 1996).

From this simulation, time series of volume transport across the IFR have been generated. These time series include the total Atlantic water flow across the ridge and also the flow split into two branches: 1) the Eastern branch crossing the south-eastern part of the ridge, and 2) the Western branch crossing the north-western part. Low passed variations of these two branches as well as their sum (total simulated) are shown in Figure 5.1 together with the observed transport through the N-Section.

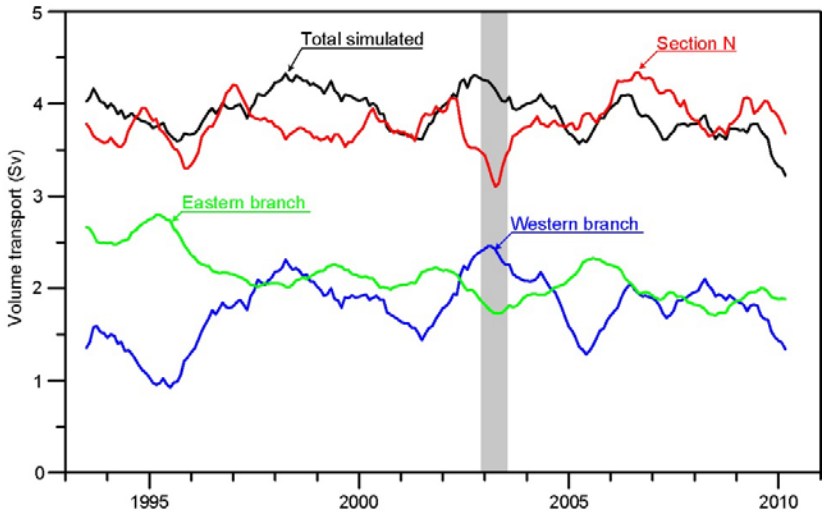

Figure 5.1. Lowpassed (12 month running mean) volume transport from simulations with the low-resolution NEMO model and as observed. The gray column indicates the 2002-2003 period with exceptionally weak observed transport through the N-Section.

As noted by Olsen et al. 2016, there is not a good correspondence between simulated and observed total transport, but the variations in the simulated Eastern branch transport bears some resemblance to the observed flow through Section N, at least during the 2002-2003 exceptional period (Figure 5.1). If, however, we compare the blue and green curves in Figure 5.1 to the similarly coloured curves in Figure 3.4, we see no correspondence and the same message is seen in Table 5.1. In this table, the temporal variations of the two simulated branches are correlated with ΔSLH over the north-western and south-eastern part of the ridge, respectively, where the splitting point between the two parts is varied. In contrast to the assessment in section 3 and 4, the two branches have comparable strength in the model.

Table 5.1. Correlation coefficients between monthly averaged ΔSLH and the transports of the two simulated branches in the low-resolution NEMO model. In the table, the series of altimetry grid points S_1 to S_{10} is split into two parts at one of the points from S_2 to S_9. For each of these splitting points, the top row shows the correlation between the transport of the Western branch and ΔSLH from S_1 to the splitting point, whereas the bottom row shows the correlation between the transport of the Eastern branch and ΔSLH from the splitting point to S_{10}.

Splitting altimetry point:	S_2	S_3	S_4	S_5	S_6	S_7	S_8	S_9
Correlation Western branch:	0.20*	0.14	0.10	0.09	0.17*	0.14*	0.13	0.21**
Correlation Eastern branch:	-0.28*	-0.31**	-0.27*	-0.21*	-0.01	0.14	0.18*	0.13

If the two simulated branches really represented volume transport across the two parts of the ridge in nature, we would have expected that there was one splitting point – preferably mid-ridge – at which the correlation coefficients for both branches were positive and reasonably high, but that is clearly not the case.

5.3 Intercomparison for the high-resolution HYCOM model

The HYCOM model grid in this simulation has a horizontal resolution ≈ 10 km and hybrid vertical grid with z-levels at the top and density levels at depth. The model simulation was initialized in 1997, but the first 10 years are considered spin-up and are subjectively disregarded for intercomparison.

From this simulation, time series of monthly averaged transport across the IFR and through the N-section have been generated for the period 1 January 2007 to 31 December 2015. The transport across the IFR was split into three subsections (Figure 5.2) yielding three time series for Atlantic water crossing

the IFR: the western branch with transport $T_{IW}(t)$, the central branch with transport $T_{IM}(t)$, and the eastern branch with transport $T_{IE}(t)$. The transport of the Faroe Current was simulated as the transport through the N-section, $T_N(t)$ (Figure 5.2).

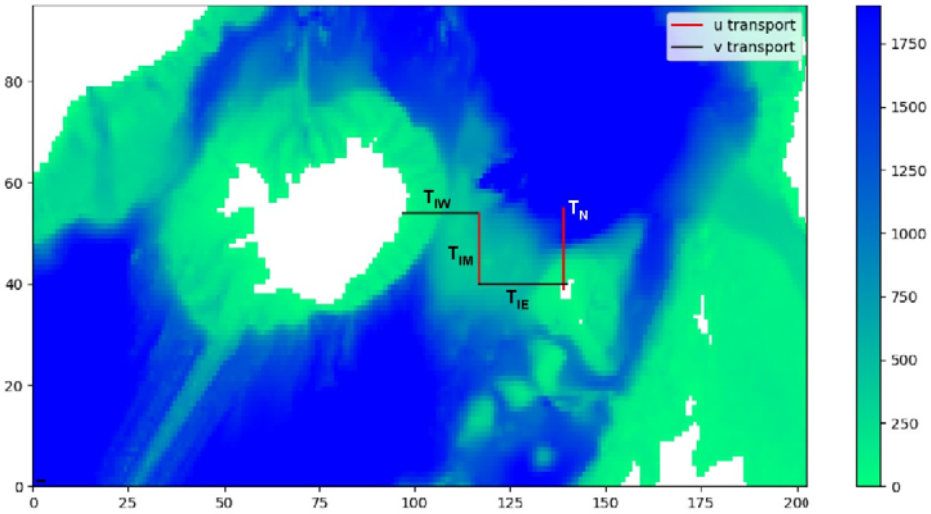

Figure 5.2. Bathymetry in the HYCOM grid with the sections, through which transports have been calculated.

Two different criteria were used to identify the Atlantic water component of the transport series. Using density ($\rho < 1027.8$ kg m^{-3}) gave a fair correlation between simulated $T_N(t)$ and observed transport through the N-section ($R = 0.45$), but the average simulated transport was much higher than the observed and the simulated transport appeared to drift. This was also evident in temperature at depth. The high model transport estimate may imply that the distinction between upper and intermediate flow was not well captured.

Using instead salinity to identify the Atlantic water ($S > 35.0$), there was no indication of a drift as this property has been nudged to climatology and the average simulated transport (3.9 Sv) was very similar to the observed average (3.8 Sv). The correlation coefficient between monthly averaged simulated and observed transport was, however, only 0.12. Applying longer averages did not reveal enhanced consistency. The seasonal cycle in the model estimate was weak consistent with observations but phases not comparable.

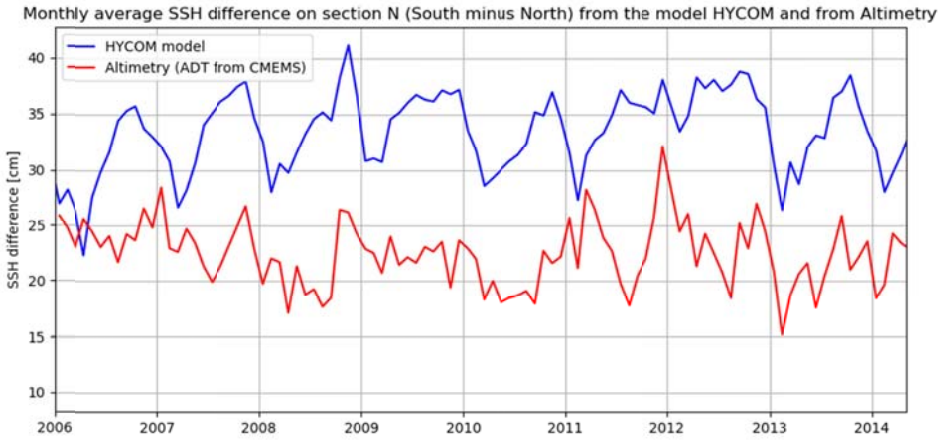

Figure 5.3. Direct comparison of HYCOM SSH difference across the N-section and Absolute Dynamic Topography from altimetry.

A comparison of simulated and observed ΔSLH across the Faroe Current (Figure 5.3) is not very encouraging. The simulated ΔSLH is on average considerably higher than the observed ΔSLH, implying considerably higher average surface currents. Also, the simulated ΔSLH appears to have a much stronger seasonal variation than the observed ΔSLH.

As a final check of the HYCOM simulation, we have correlated the simulated transport series through the three sub-sections on the IFR (Figure 5.2) with sea level differences between various pairs of altimetry points. For the central branch, we could not find any interval between altimetry points with significant positive correlation. We have therefore defined two new simulated transport series by adding the transport of the central branch either to the western branch or to the eastern branch, labelled $T_{IN}(t)$ and $T_{IS}(t)$, respectively. In Table 5.2, we have split the IFR into a northern part with sea level difference $\Delta H_N(t)$ and a southern part with difference $\Delta H_S(t)$ and varied the splitting point to see the effect on correlations.

From the table, the best correlations are obtained if the splitting point is close to the northwestern end of the altimetry section (at points S_2 or S_3), in which case there are some statistically significant positive correlations. They are not high, however. Eastern transports tend to be more stable (not shown) and with a higher mean value than transports to the west. Drift in the model does however limit our ability to verify the observational assessment of a dominant flow to the east (Figure 3.5, Section 4).

Table 5.2. Correlation between monthly averaged sea level difference over either the northern (ΔH_N) or the southern (ΔH_S) part of the IFR from altimetry and simulated (by HYCOM) transport of branches. Splitting point is the altimetry point dividing the northern and the southern part (Figure 2.1). T_{IW} is the simulated western branch, T_{IE} is the simulated eastern branch. $T_{IN} = T_{IW} + T_{IM}$, $T_{IS} = T_{IE} + T_{IM}$, where T_{IM} is the simulated central branch.

Splitting point	ΔH_N T_{IW}	ΔH_S T_{IE}	ΔH_N T_{IN}	ΔH_S T_{IS}
S_2	0.30**	0.35	0.20	0.24*
S_3	0.25*	0.37	0.21	0.23*
S_4	0.13	0.30	0.16	0.16
S_5	0.09	0.25	0.10	0.15
S_6	0.05	0.12	-0.01	0.12
S_7	0.10	-0.00	-0.05	0.14
S_8	-0.03	-0.17	-0.09	-0.02
S_9	0.06	0.03	-0.03	0.12

5.4 Intercomparison for the ORAS5 reanalysis

In order to build additional confidence in our conclusion on model discrepancies against observations and to develop our conclusions, we choose to complement the model data from the HYCOM model by another relatively high resolution model product, the ORAS5 reanalysis (Zuo et al. 2019, in discussion). As in O2016, this ocean product is also based on the NEMO ocean model which has a fundamentally different architecture than HYCOM (z-level vs. hybrid coordinates). Compared to O2016, the resolution of ORAS5 is four times higher in both meridional and zonal direction and almost doubled in the vertical (75 layers). In this region, ORAS5 may be considered eddy permitting. Also, this product is informed by full depth ocean observations, not simply forced (atmosphere) at the surface (O2016). Hence, this model does not suffer from a spurious drift in any state variables. ORAS5 also offers an ensemble of perturbed initial conditions with five members. This allows a direct assessment of model uncertainty. Importantly, observational data from transport mooring arrays (e.g. section-N ADCP's) have not been considered in the ORAS5 assimilation system but altimetry products have with some weight. Therefore a number of the consistency checks performed on the unconstrained HYCOM model regarding SSH are less informative or relevant to conduct for ORAS5.

With ORAS5 we seek to demonstrate first that diagnosed AW transport on the N-section is indeed a robust estimate of the inflow across the IFR. This is apparent from Figure 5.4 showing for all five

ensemble members a good correspondence between the flow across the IFR and the flow on the N-section. This includes a correlation of 0.5 to 0.6 across the ensembles and a modest water mass entrainment increasing the property constrained transport estimate by 0.1 to 0.2 Sv from IFR to FN. The average transport is about 10-15% lower than the observed transport.

This is extremely encouraging as it indirectly supports the observational practice to monitor the flow on section-N. Despite the high average consistency of flow over the IFR with transport on the N-section, none of the ensemble members shows a temporal variability that compares well with observations on the N-section. This is reflected by low correlation coefficients (between 0.09 and 0.23 for the simulated inflow on the N-section). Interestingly, also the ensemble average transport is poorly correlated with the observed transport and weaker than individual members (0.18). This may be seen as a first indication of a prominent role of internal ocean variability compared to forced variability in the IFR exchange system. Even internal correlation between ensemble members is not high (see also Figure 5.4). The ensemble spread and discrepancies indicates that the IFR ocean exchange system is not (or cannot be) constrained in the ORAS5 ocean reanalysis system by the available in-situ observations (in situ and EO). As such, there is a critical need for continued, robust observational estimates (monitoring) of the transport across the IFR.

To get a perspective on the level of model uncertainty in AW transport across the IFR, statistics of the N-Section time series can be compared with AW transport in the Faroe Shetland Channel (FSC). Figure 5.5 shows the time series of observed and simulated transport of Atlantic Water, diagnosed from the ORAS5 ensemble as the transport above 500 m. Simulated transport compares very well with observations (again an estimate incorporating altimetry) for all ensemble members (correlations between 0.68 and 0.75). Furthermore, the five ensemble members are very similar with an average member-to-member correlation of > 0.9. For the AW transport on the N-section (or on IFR) in contrast, the ensemble members correlate with each other only by 0.76 (0.75). This finding of elevated uncertainty is supported by assessing the ensemble spread: On the N-section, the standard deviation between ensemble members based on normalized time series is 60 % higher than in the FSC. The same relations are found for the deep water flow in the FSC. This additionally supports our perception that the inflow of AW on the IFR (and the N-section) is weakly constrained.

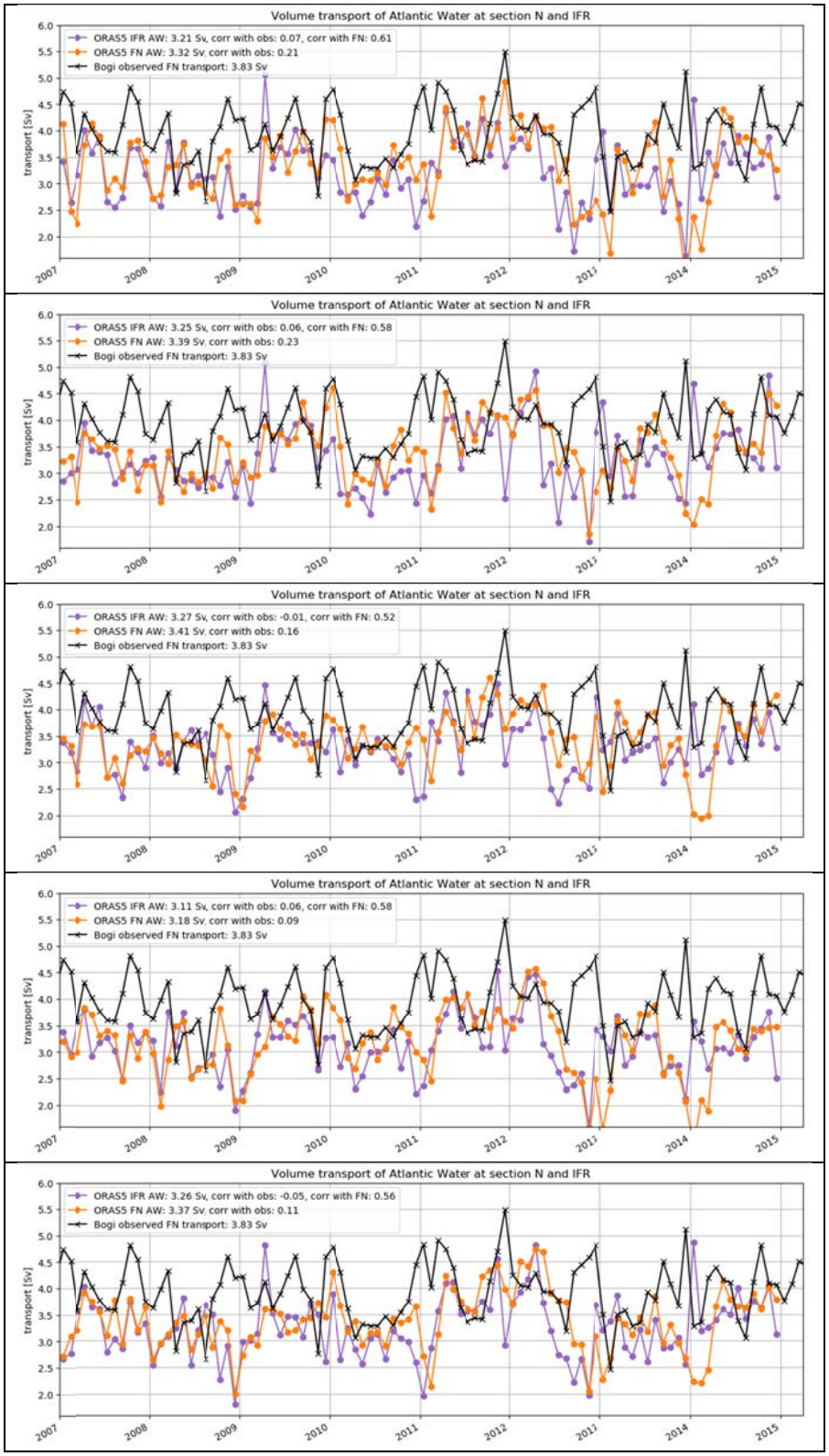

Figure 5.4. Simulated (ORAS5) Atlantic Water transport across the IFR (blue) and section-N (orange) in five individual ensemble realizations of the flow compared against observational results at the N-section.

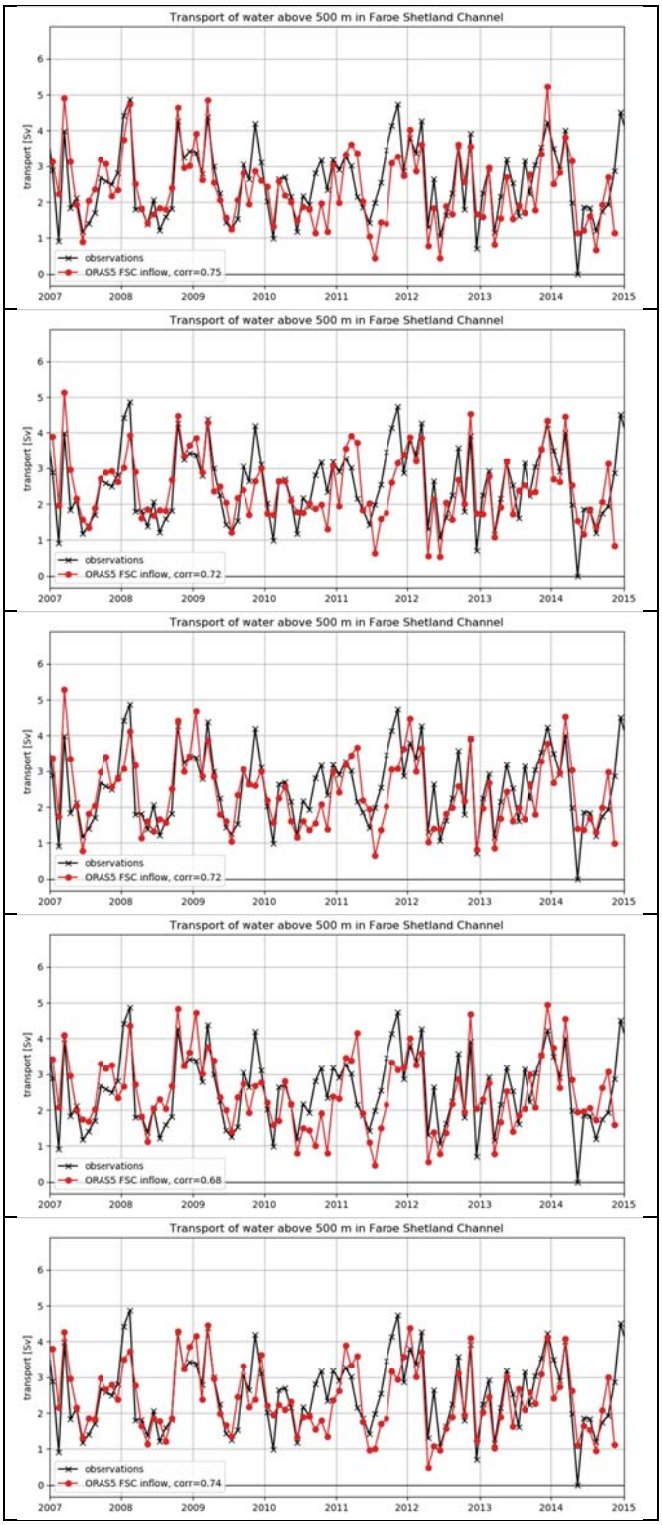

Figure 5.5. Simulated (ORAS5) Atlantic Water transport across the FSC (red) in five individual ensemble realizations of the flow compared against observational results (black, www.OceanSites.org).

That the AW transport on the N-section as well as on the IFR is less constrained in the ORAS5 than other key branches of inflow implies either a strong role of internal ocean variability or, that the net

driving forces are less robust. The latter may be the case exactly if the net flow is a small residual of stronger compensating flows (and compensating forces). This idea finds support in an apparent weak relation of the net transport to simple SSH metrics (Figure 5.6) - the flow across the IFR does not respond to the pressure gradient across the IFR. Also, the AW transport on Section-N is not well described by the surface sea level slope alone, in contrast to the direct observational based result on section-N.

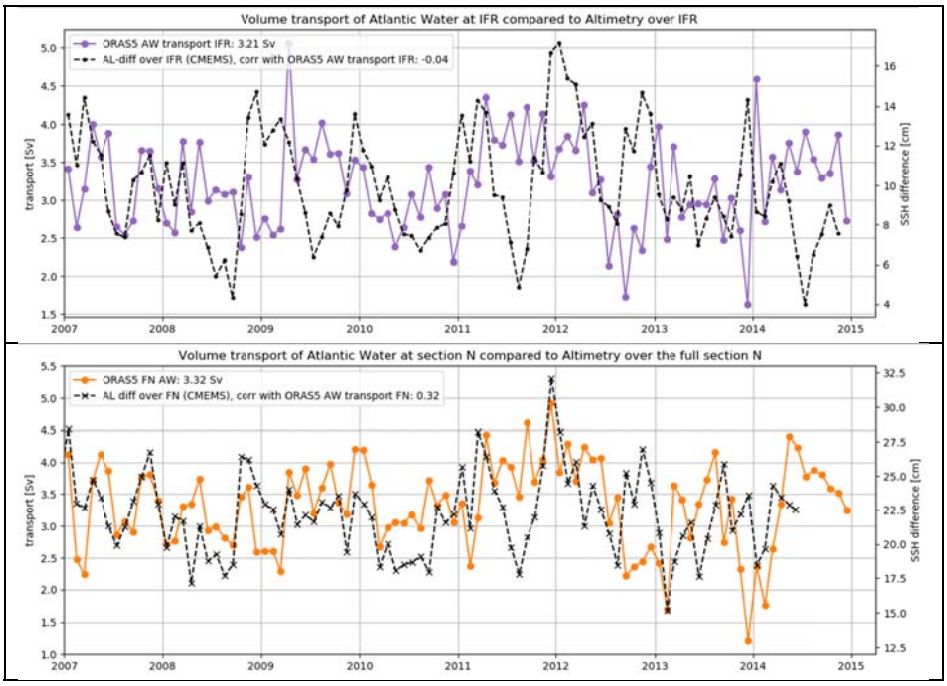

Figure 5.6. Relations between simulated (ORAS5, single ensemble) Atlantic Water transport SSH derived metrics describing flow or forcing. Top: Atlantic Water transport across the IFR (purple) and the SSH gradient across the centre part of the ridge. Bottom: Atlantic water transport on the N-section (orange) and the SSH gradient across the full section (black, dashed).

The model simulated AW transport over the IFR is not well described by the gradient in sea-surface height across the ridge. Such a relation has however been indirectly verified by observational results on the N-section. In addition, ORAS5 transport on the N-section is also only weakly correlated to the full gradient in sea-level across the section (r>0.3).

Discrepancy between model and observations can also be identified in the seasonality of the transports. In Figure 5.7 we compare yearly cycles not only of Atlantic water transport on the N-section, but also with the deep circulation on the section. We define deep water (DW) as water colder than 1^{o}C and deeper than 350m. As for the direct comparison of monthly mean variability (Figure 5.4), there is no correspondence between observed and simulated seasonality on section-N. Noteworthy is however the consistent seasonal cycle on the IFR and on the N-section. When turning to the estimate of the deep water transport on the N-section, the apparent alignment of phase between the simulated DW and observed AW transport is striking. The amplitude of simulated DW seasonality is higher than in the upper layer (observed), but the absolute level is somewhat arbitrary and linked to the chosen extent of the section. The relatively strong seasonality explain in part a high correlation (r=0.57, not shown) between monthly averages of the two supposedly independent transports. A similar results but less robust could be demonstrated with HYCOM and as explained above, O2016 noted the apparent connection focussing on a particular strong seasonal anomaly. However, neither with HYCOM data nor in O2016, a close relation between AW flow on the IFR and FN could be demonstrated. Now, integrating ORAS5 ocean reanalysis data, it can be concluded that if model errors account for the discrepancy

against observations, they are linked to the simulated transport across the IFR. This could be linked to poor representation of the deep circulation in the Nordic Seas whereby also the dominant seasonality of flow across the IFR is not resolved.

If the variability including seasonality in the deep and intermediate transports along the northern flank of the IFR is coupled to vertical displacement of the interface between AW and DW, we may expect that even small biases in the model interface depth can either exaggerate or eliminate seasonality in the inflow across the IFR by a number of processes (but likely not via overflow in the Western Valley). Such mechanisms would also be consistent with the results from the analysis of the ORAS5 ensemble, showing that the AW transports are relatively poorly constrained. We conclude also that it is critical to separate with skill the interface between AW and DW on section N to avoid the strong (seasonal) fluctuations of transports at depth to pollute the estimate of upper transports.

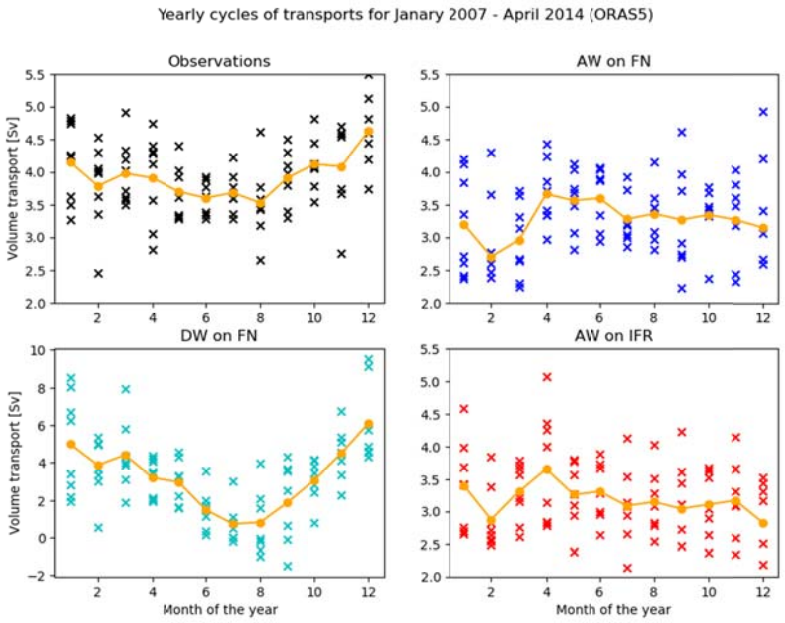

Figure 5.7. Seasonal cycle of transport of AW on the N-section from observations (upper left), from ORAS5 on the N-section (upper right) and across the IFR (lower right). Also shown is the transport of deep water (DW) on the N-section (lower left).

The ORAS5 results are a-priori expected to better represent ocean dynamics (eddy permitting) compared to the O2016 data. The two datasets differ also due the assimilation of ocean data and earth observations in the ORAS5 reanalysis. It cannot be excluded that the assimilation procedures are not well suited for the purpose of constraining the IFR inflow, possibly by interfering with the deep circulation in the Nordic Seas. Some evidence suggests that the data should be used with some caution. First, the Atlantic inflow has been calculated on an alternative section on the IFR which cut through the different branches on the western part of the IFR. Enhanced recirculation should be expected, but near identical AW transport would be expected, but significant differences are found that seem to exceed previous mentioned ranges of entrainment as the AW progress towards the N-section. Figure 5.8 shows the “new” (red) and “old” (green) sections (old section used above).

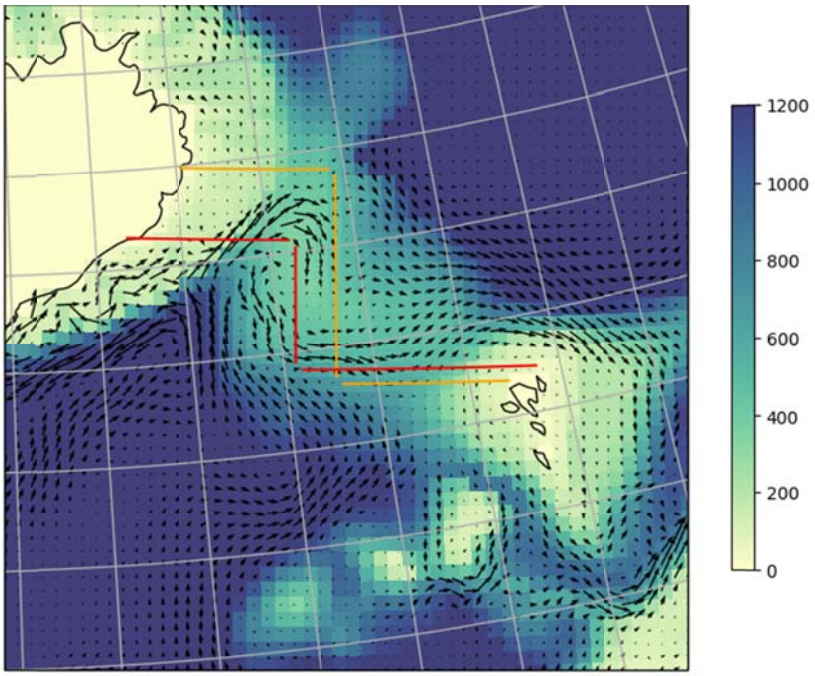

Figure 5.8. Bathymetry[m] and average surface currents in ORAS5 (single memnber) on the IFR. The section used for calculating transports is shown in green. An alternative "new" section following close the ridge and crossing the Western Valley in red.

On the section, the vertical velocity profile (total transport velocity, see Figure 5.9 for a monthly snapshot) is almost barotropic and bottom intensified in some regions or periods, features which are not necessarily supported by observations. Occasionally, inflow is only found at the bottom most grid cell on the eastern part of the IFR (not shown). Still, the general flow distribution including surface currents is consistent with the pattern derived from observations on the ridge (Figure 3.5). This includes a main inflow branch in the region of the Western Valley with a significant recirculation loop as well as a more diffuse eastern inflow (see Figure 5.8 and 5.9). The western branch and its recirculation is captured by the western and centre segments, the eastern inflow branch by the in the centre segment of the "new" IFR section.

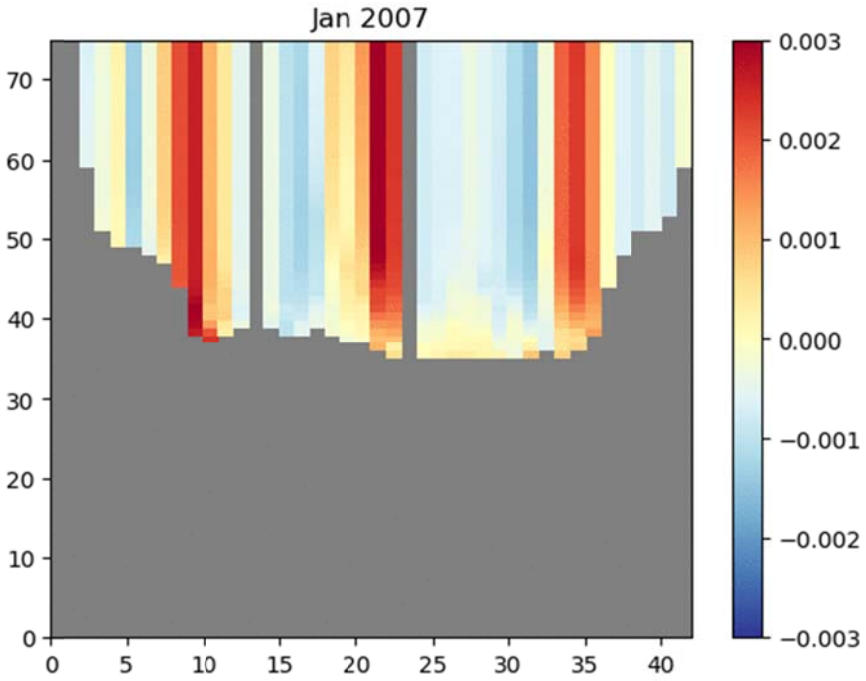

Figure 5.9. Vertically and horizontally binned ORAS5 transport velocity [m^2s^{-1}] according to the model grid for January 2007 (single member) along the "new" IFR cross-section (left=west, right=east). Horizontal axis is grid number, vertical axis model levels.

The new section is used to construct a Hovmöller diagram of vertically integrated transport on the IFR, divided into its three segments, west, center and east (Figure 5.10). The distinct western inflow branch and its recirculation on the center segment are easily identified and stationary according to the vertical averages. The eastern inflow is here seen to be more diffuse than seen in the snapshot (Figure 5.9). The diffuse nature is consistent with the analysis of available observations. It is noted that less inflow on western branch around September is often compensated by less outflow in the center segment. On the western and center segments, total inflow and outflows are strongly anticorrelated as would be expected. Net inflow through the western segment is almost twice as large as the total inflow on the two segments defining the western branch. This ration has not been assessed in the above analysis of available observations. Focusing on the net inflow, the two branches are of comparable magnitude in contrast to observations which indicate that the diffuse eastern inflow is about three times larger than the net inflows to the west. These differences could of course also explain the lack of consistency with observed seasonality or temporal variability (Figure 5.4 and 5.7).

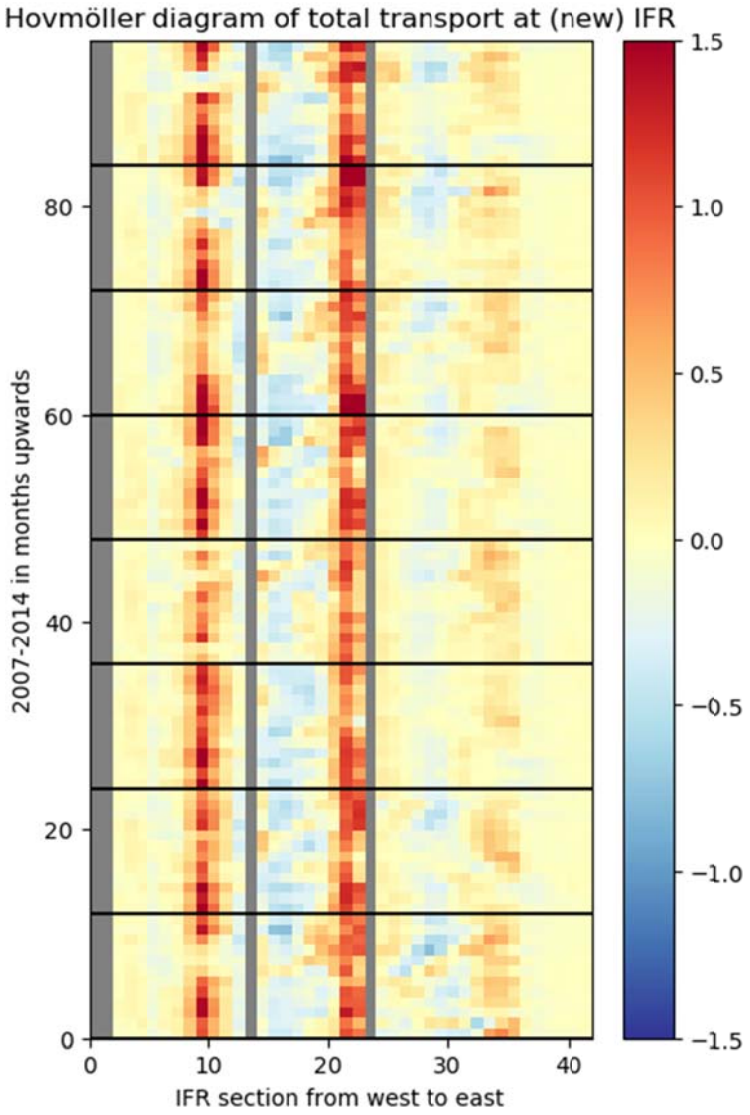

Figure 5.10. Hovmüller diagram of the vertically integrated total transport [Sv] on the IFR (ORAS5, single member, 2007-14). The three subsections seen in Figure 5.8 are separated by a grey column. The western branch is defined as grid cells 7:11 and the eastern branch as grid cells 20:22 along the IFR section. Black horizontal lines indicate Januaries.

5.5 Eddy permitting to eddy resolving model systems

It is possible that the eddy permitting resolution of both the ORAS5 reanalysis and the HYCOM output is still a limiting factor for realistic simulation of the IFR exchange system. To directly address the possible importance of resolution, two comparable simulations are introduced based on the same ocean general circulation model (NEMO). These are in contrast to the reanalysis only constrained by surface forcing (DRAKKAR) and differ in nominal resolution, being 1/12 and 1/24 degrees, respectively. The oceans most energetic scales will be adequately resolved in the 1/24 degree setup. Figure 5.11 shows the seasonal cycle of the net inflow, total inflow and total outflow on the IFR inflow. Time-series of these three components are also included and the net transport across the IFR can be compared with the observed AW transport on section-N. For simplicity, we use the total, vertically integrated flow to represent the AW exchanges as there is no significant overflow of cold, dense water on the IFR in these two simulations.

The net, total inflow in both simulations is one third lower than observed inflow of AW at section-N, but relatively free of model drift stable as the observed record. Focussing on the 1/12 degree simulation, a robust average seasonal cycle with significant amplitude can be identified with a minimum in summer and maximum during fall and winter. Simulated seasonality and amplitude compares relatively well with the seasonality of observed AW inflow on section-N, in contrast to the analysis of the assimilated ORAS5 results above (same nominal resolution, Figure 5.7). Seasonality is seen to result from largely compensating contributions where the seasonality of the net transport is dominated by the cycle of the inflow and with the same phase. Time-series of total inflow, outflow and the net transport suggests that the net inflow consisting of mainly AW is only roughly 1/3 of the total inflow so that 2/3 is recirculating back across the ridge. Similar rations were discussed for ORAS5 above. Direct correlations of simulated transport diagnostics should be affected by this seasonality, but still found to be low. Despite a close correlation, these results on seasonality are highly encouraging. However, enhancing resolution in the eddy resolving simulation (1/24) does not improve the comparison. Total inflow and outflow is still anticorrelated and contribute to the seasonality of the net flow. Amplitudes are noticeably weaker compared to the 1/12 degree simulation. In contrast, the time-series show a significant increase in recirculation going from 1/12 to 1/24 degree indicating that new dynamics are reproduced.

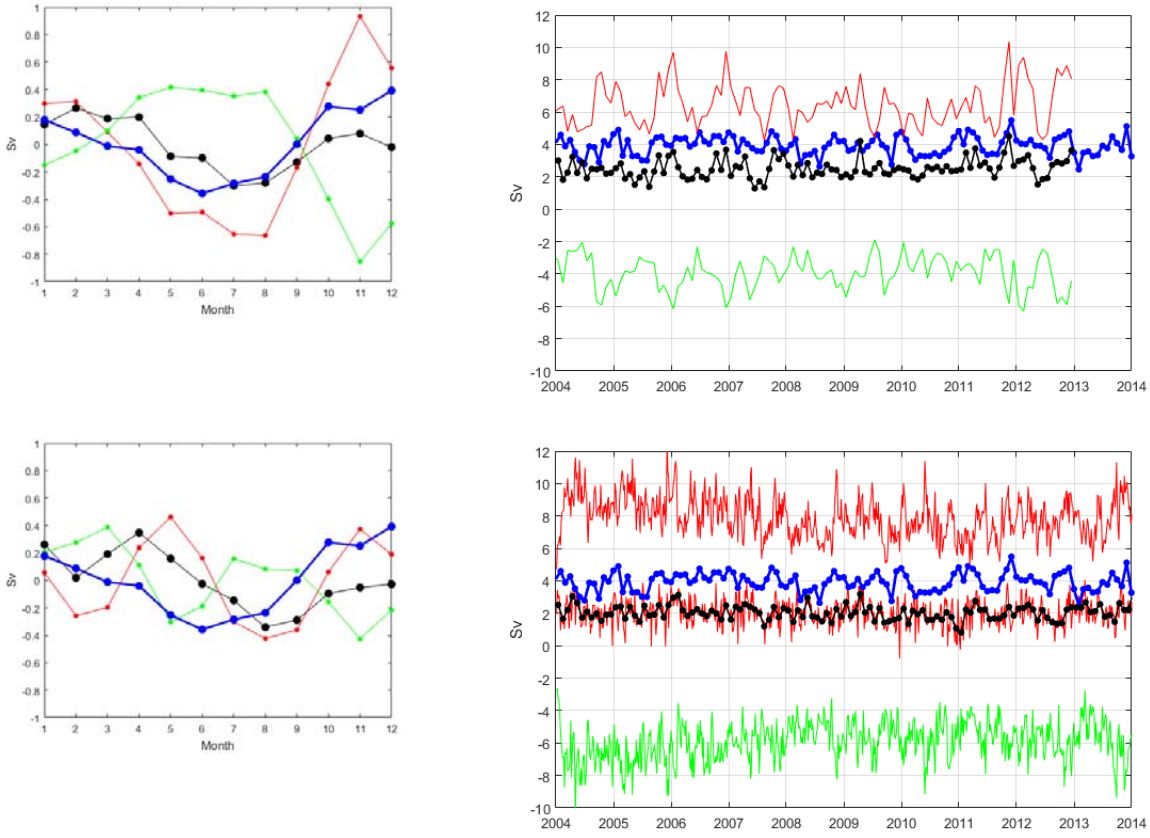

Figure 5.11 Seasonal cycle (left) and time series (right) of transport of AW on the IFR from two NEMO ocean configurations 1/12 (top) and 1/24 (bottom) degree resolution. Net inflow (black) is compared with observations at the N-Section (blue). Also shown is the total inflow (red) and total outflows (green).

5.6 Conclusions

In summary, the eddy permitting simulation using the 1/12 degree model configuration show for the first time a seasonality of the inflow across the ridge consistent with observations and, as a residual of two strong seasonal signals. Increasing resolution enhances recirculation on the IFR, but does not necessarily result in improved comparison with observed AW inflow. The ratio of recirculation is sensitive to the sections defined as well as resolution. Ocean reanalysis ensemble data indicate that internal ocean variability is an important driving mechanism for observed changes in the inflow. The forced variability emphasized in the ensemble mean does not present a superior fit with observations compared to individual ensemble members. It can is likely that internal variability involves also deep circulation in the neighbouring seas. Low general correlations of initialised ensemble members indicate that available observations are not sufficient to constrain the IFR inflow and the internal variability that control its variability. Alternatively, the assimilation methods interfere negatively with part of the dynamics describing the IFR exchange system. Combined, these results suggests that adequately tuned ocean models of eddy permitting resolution are sufficient for simulating the main characteristics of the IFR inflow including horizontal structure, individual characteristics of the two branches as well as seasonality of the net transport.

Progress beyond the state of the art

The work offers the most complete compilation of available observational data to shed light on the structure of the flow across the Iceland-Faroe Ridge carrying half of the ocean heat transport to the Arctic. The proposed circulation consisting of a recirculating loop of Atlantic water with main inflow east of Iceland and a more sluggish, diffuse eastern branch is supported by and consistent with all available observations and qualitatively supported by the newest ocean reanalysis data. Apparent discrepancies with ocean general circulation models are addressed by also including ultra-high resolution ocean simulations.

Impact

How has this work contributed to the expected impacts of Blue-Action?

Improve capacity to predict the weather and climate of the Northern Hemisphere, and make it possible to better forecast of extreme weather phenomena

Improve the capacity of climate models to represent Arctic warming and its impact on regional and global atmospheric and oceanic circulation

Lead to optimised observation systems for various modelling applications

Improve the uptake of measurements from satellites by making use of new Earth observation assets

Climate models have been shown to have limited skill in simulating the ocean exchanges in complex oceanographic settings. Results contribute to understand the suitability and utility of the ocean observing system for initializing prediction systems. Targeting the important Iceland-Faroe Ridge inflow to the arctic, present limitations in constraining or initializing the regional ocean exchange system are demonstrated by use of reanalysis data assimilating available observations in combination with unassimilated but realistic simulations.

By addressing the limiting factors for simulation of the IFR the results directly impact on improved representation of Arctic-lower latitude ocean linkages. Narrowing down the critical limiting range of ocean process realisms needed to realistically simulate the exchanges (including heat anomaly propagation modulating Arctic sea-ice) is a significant advancement. In turn, this will also help to improve the representation of Arctic warming and its impact on regional and global scales.

Impact on the business sector

Strengthening the competitiveness and growth of companies by developing innovations meeting the needs of European and global markets; and, where relevant, by delivering such innovations to the markets

Improve the capacity to respond to the impact of climatic change on the environment and human activities in the Arctic, both in the short and longer term

Improving innovation capacity and the integration of new knowledge

Contribute to better servicing the economic sectors that rely on improved forecasting capacity

Improve stakeholders' capacity to adapt to climate change

Intensive fisheries in the productive region of the Iceland-Faroe Ridge as well as the consolidated aquaculture industry and new blue bio-economies will directly and indirectly benefit from improved simulation and predictions of the flow towards the Arctic. Experimental ecosystem or fisheries forecasts and related climate services (WP5) will be essential tools to facilitate the uptake of improved predictive capacity of ocean currents.

Lessons learned and Links built

- An unexpected important legacy of this activity is the compilation and expected publication of available an unexploited observational data relevant for the topic.

- Linkages to PRIMAVERA have been exploited to achieve the goals of this deliverable. The work in Blue-Action will feed back on joint interests in assessment of ocean model simulations.

Contribution to the top level objectives of Blue-Action

This deliverable contributes to the achievement of the following objectives and specific goals indicated in the Description of the Action, part B, Section 1.1: http://blue-action.eu/index.php?id=4019

Objective 2 Enhancing the predictive capacity beyond seasons in the Arctic and the Northern Hemisphere

By addressing the simulation of an important component of the Atlantic Meridional Overturning circulation and ocean teleconnections between the arctic and lower latitudes.

Objective 5 Optimizing observational systems for predictions

By addressing the adequacy of present ocean observations to constrain in ocean reanalysis systems the exchange system in the region of the IFR which will be key for skilful predictions.

Objective 6 Reducing and evaluating the uncertainty in prediction systems

By addressing the adequacy of present ocean observations to constrain in ocean reanalysis systems the exchange system in the region of the IFR which will be key for skilful predictions.

References (Bibliography)

- Hansen, B., Østerhus, S., Hátún, H., Kristiansen, R., and Larsen, K. M. H.: The Iceland–Faroe inflow of Atlantic water to the Nordic Seas, Prog. Oceanogr., 59, 443–474, doi:10.1016/j.pocean.2003.10.003, 2003.
- H2015. Hansen, B., Larsen, K. M. H., Hátún, H., Kristiansen, R., Mortensen, E., and Østerhus, S.: Transport of volume, heat, and salt towards the Arctic in the Faroe Current 1993–2013, Ocean Sci., 11, 743–757, https://doi.org/10.5194/os-11-743-2015, 2015.
- Hansen and Larsen, 2019 (in prep). Monitoring the velocity structure of the Faroe Current. Havstovan Technical Report no. 19-01.
- Kalnay, E., Kanamitsu, M., Kistler, R., Collins, W., Deaven, D., Gandin, L., Iredell, M., Saha, S., White, G., Woollen, J., Zhu, Y., Chelliah, M., Ebisuzaki, W., Higgins, W., Janowiak, J., Mo, K.C., Ropelewski, C., Wang, J., Leetmaa, A., Reynolds, R., Jenne, R., Joseph, D., 1996. The NCEP/NCAR 40-year reanalysis project. Bulletin of the American Meteorological Society 77 (3), 437–471.
- O2016. Olsen, S. M., Hansen, B., Østerhus, S., Quadfasel, D., and Valdimarsson, H.: Biased thermohaline exchanges with the arctic across the Iceland-Faroe Ridge in ocean climate models,
- Ocean Sci., 12, 545–560, https://doi.org/10.5194/os-12-545-2016, 2016.
- Pyper, B. J. and Peterman, R. M.: Comparison of methods to account for autocorrelation in correlation analyses of fish data, Can.J. Fish. Aquat. Sci., 55, 2127–2140, https://doi.org/10.1139/f98-104, 1998.
- Østerhus, S., Woodgate, R., Valdimarsson, H., Turrell, B., de Steur, L., Quadfasel, D., Olsen, S. M., Moritz, M., Lee, C. M., Larsen, K. M. H., Jónsson, S., Johnson, C., Jochumsen, K., Hansen, B., Curry, B., Cunningham, S., and Berx, B.: Arctic Mediterranean Exchanges: A consistent volume budget and trends in transports from two decades of observations, Ocean Sci. Discuss., https://doi.org/10.5194/os-2018-114, in review, 2018.
- Zuo, Hao & Balmaseda, Magdalena & Tietsche, Steffen & Mogensen, Kristian & Mayer, Michael. (2019). The ECMWF operational ensemble reanalysis-analysis system for ocean and sea-ice: a description of the system and assessment. Ocean Science Discussions. 1-44. 10.5194/os-2018-154.

Dissemination and exploitation of Blue-Action results

Peer reviewed articles

Title	Authors	DOI	Is Blue-Action correctly acknowledged?	Status?	Open Access granted
Overflow of cold water across the Iceland–Faroe Ridge through the Western Valley	Bogi Hansen, Karin Margretha Húsgarð Larsen, Steffen Malskær Olsen, Detlef Quadfasel, Kerstin Jochumsen, and Svein Østerhus	https://doi.org/10.5194/os-14-871-2018 https://www.ocean-sci.net/14/871/2018/	Yes	Published	Yes

Uptake by the targeted audiences

As indicated in the Description of the Action, the audience for this deliverable is the general public (PU) is and is made available to the world via CORDIS.

This is how we are going to ensure the uptake of the deliverables by the targeted audiences:

The results are disseminated to the scientific community through participation to meetings and workshops.
The full track of the dissemination activities linked to this deliverable and the other deliverables in WP2 is reported in the second periodic report.
The results are included in a draft of a scientific publication, to be submitted to a peer reviewed journal in 2020.